# Ringing mountain ranges: Teleseismic signature of the interaction of high-frequency wavefields with near-source topography at the Degelen nuclear test site

**Marta Pienkowska**[1, 2], **Stuart E. J. Nippress**[3], **David Bowers**[3], and **Tarje Nissen-Meyer**[2,4]

[1]Department of Earth Sciences, ETH Zurich, Zurich, Switzerland.
[2]Department of Earth Sciences, University of Oxford, Oxford, UK.
[3]AWE Blacknest, Brimpton, Reading, UK.
[4]Department of Mathematics and Statistics and Joint Center of Excellence in Environmental Intelligence, University of Exeter, Exeter, UK

## Abstract

Over the last decade there has been an international effort to find methods to recover and digitize recordings from historical earthquakes and explosions that occurred during the 1950's through to the 1980's. Making these recordings accessible in digital format offers opportunities to study what signatures are encoded in the data, and to apply state-of-the-art techniques and methods to historical data. In this study we employ unsupervised machine learning to cluster historical teleseismic waveforms from nuclear explosions conducted at the former USSR Degelen test site, in Kazakhstan, recorded at seismic arrays in the UK (EKA), Canada (YKA), Australia (WRA) and India (GBA). In particular, we use two unsupervised algorithms to cluster waveforms using shape-based clustering: kernel k-means and k-Shape. The algorithms clearly split waveforms into distinct clusters that are spatially related, even when waveform differences are subtle, and we show with local and teleseismic numerical simulations that the clusters are related to the topography. The topography at the Degelen test site has characteristic wavelengths of 2-4 km and local simulations highlight that the seismic wavefield is trapped in reverberating mountain peaks. The location of the explosion is crucial in determining which section of the mountain range reverberates, influencing the outgoing wavefield. Teleseismic waveform simulations confirm that it is this superposition of energy leaving the reverberating peaks that results in the observed teleseismic waveform differences we observe.

**Keywords** machine learning · time-series analysis · wave propagation · wave scattering and diffraction · numerical solutions · body waves

## 1 Introduction

The influence of the near-source region on the observed characteristics of seismic waveforms is well documented [e.g., 21, 46, 60]. Factors such as source depth and magnitude, near-source scattering from topography or shallow geological structural heterogeneities, as well as local non-linear effects can all impact the complexity of observed waveforms. During the late 1980s and early 1990s, near-source contributions to teleseismic P-waves and early coda waves were analysed for a number of underground explosion sites [e.g., 17, 27, 28, 32, 35, 36], however it is often difficult to unambiguously determine the dominant contributing factors through data analysis alone.

Over the last decade there has been an international effort to find methods to recover and digitize recordings from historical earthquakes and explosions that occurred during the 1950's through to the 1980's [e.g., 59]. With new processing techniques and numerical methods at hand, revisiting the digitised data from underground nuclear explosions could bring valuable insights into near-source interactions that are observed at teleseismic distances. Unlike naturally occurring seismicity, seismic waveforms from historical nuclear tests have well known source locations, magnitudes, near-source geology and topography. Therefore, they provide an ideal starting point for a systematic and rigorous analysis to understand the different near-source contributions to teleseismic waveform characteristics.

Previous studies have suggested that the interaction of the seismic wavefield from nuclear explosions with near-source topography is a key cause of waveform variations observed from a single test site [e.g., 17, 18, 19, 32, 35, 36, 46, 54, 58]. Numerical simulations have concentrated on the effect of topography on seismic wavefields at local–intermediate distances or at teleseismic distances in 2-D, thereby significantly reducing the propagation complexity and possibly ignoring important 3-D effects. Topographic effects on local wavefields were also studied in the context of crustal earthquakes [e.g., 53], volcano seismology [e.g., 26, 44], and ground motions for seismic hazard assessment [e.g., 3, 10, 21, 22, 24, 29, 33, 34, 43, 60]. These studies demonstrate that topographic scattering is significant at short distances provided the length scale of the topography is comparable to the seismic wavelength, although the effects are more variable in the presence of steep slopes. However, whether near-source topography scattering can be detected at teleseismic distances has been difficult to test.

In this study we analyse teleseismic waveforms from nuclear explosions conducted at the former USSR Degelen test site, in

*correspondence: marta.pienkowska@erdw.ethz.ch
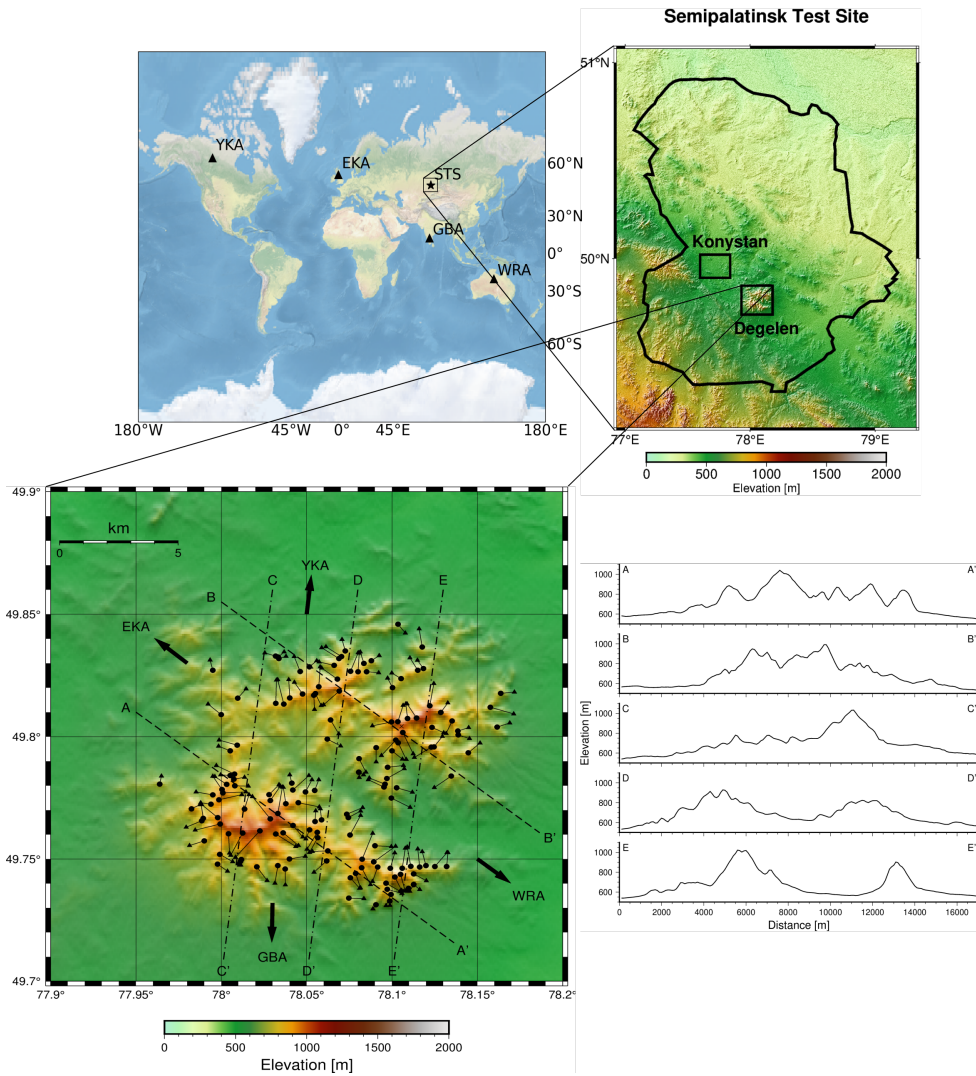
Figure 1: Location of the STS (star) and Degelen mountain test sites and the four UK-design arrays used in this study. The GBA array is 36.4° epicentral distance from Degelen, EKA 47.1°, YKA 67°, and WRA 85.3°. Adit portals (triangles) and ends (circles) [56] are plotted over the Degelen topography for data available at AWE Blacknest. Five profiles show the topographic variation across the Degelen test site.

Kazakhstan, that potentially exhibit a strong signature of near-source effects. The results of unsupervised time-series clustering show a clear dependence on source location within the Degelen mountain range. We propose that the change in signal characteristics is dominated by the near-source topography, which determines how the mountain range reverberates, resulting in a progressive change of waveform features as source location shifts along the ridges. We present results from both local and teleseismic numerical simulations for 3-D topography that demonstrate the significant effect near-source topography has on seismic waveforms.

## 2   TELESEISMIC WAVEFORM DATA FROM NUCLEAR EXPLOSIONS AT THE DEGELEN TEST SITE

In the early 1960s the UK Atomic Energy Authority (now Atomic Weapons Establishment, AWE), working closely with the host country, constructed four UK-designed seismic arrays for nuclear test monitoring: the Eskdalemuir array (EKA) in Scotland, the Gauribidanur array (GBA) in India, the Warramunga array (WRA) in Australia and the Yellowknife array (YKA) in Canada (Figure 1). These arrays have been running nearly continuously since their initial deployment and EKA, WRA and YKA now form part of the Comprehensive Nuclear-Test-Ban Treaty global International Monitoring System.

The Semipalatinsk test site (STS, Figure 1) in north-eastern Kazakhstan was the primary location for nuclear testing in the USSR. In total 456 tests were carried out at STS between 1949-1989 [20], including 214 underground tests located within the Degelen Mountain, a granitic mountain range with an area of 220 km$^2$. The majority of these explosions had yields of 4-20 kT, with a small number in the 20-125 kT range [7, 35]. All tests conducted at Degelen were in adits drilled into mountain slopes, with charges usually placed at the adit end [7].

137 Degelen explosions between 1964-1989 were recorded by the four arrays (EKA, GBA, WRA and YKA). The more recent explosions were recorded directly as digital data. However, the majority of signals were recorded on analogue magnetic tapes that have been digitised at 20 samples per second, the sampling rate used for digital recordings. In this study we analyse the vertical component beamformed signals at each array. Individual channels were manually examined and data with inconsistencies such as dropouts, excessive system noise, inverted signals, mislabelling or analogue-to-digital conversion problems, as well as recordings for simultaneous double explosions were discarded. Individual channels were then beamformed using delay-and-sum processing using IASP91 [23] slowness estimates. The directional layout of the arrays maximises the signal-to-noise ratio for events at STS, allowing a high-quality archive of seismograms from the period of underground testing. Official event locations, depths, and yields were released by the USSR for the pre-1972 tests [6]. For later tests, only estimates of event locations [30, 56] and body-wave magnitude ($m_b$) [39] are available (Table S1 in Supporting Information).

In this study we analyse only the first 20 seconds following the P-wave arrival, since beamforming techniques are designed to enhance the P-wave energy leaving the source region, and sup-press later arriving waves. We refer to the entire wave-train after the direct P arrival as the P-wave coda – our definition thus includes all scattering in the near-source region, along the path, and under the receivers. All waveforms are cut with the P-wave onset at time $t = 0$ s, normalised by the maximum amplitude, and filtered with a zero-phase low-pass Butterworth filter at 2 Hz, 4 Hz and 8 Hz.

## 3   TELESEISMIC WAVEFORM CHARACTERISTICS OF DEGELEN EXPLOSIONS

Marshall et al. [35] analysed data from eight Degelen explosions with known source parameters that were separated by up to 15 km. Despite common stations and propagation paths the analysed events show significant differences in the P-wave and its coda. Compared with signals recorded at the same arrays, but from explosions at the the flat Konystan test site (only 40 km away), the Degelen signals are remarkably complex (Figure 2). The path and receiver effects are expected to be very similar from the two test sites, indicating that something in the near-source region of the Degelen test site is generating this waveform complexity. Marshall et al. [35] attributes the observed waveform variations to the Degelen near-source region, with the waveform variability between the arrays explained by both the take-off angle and azimuth.

McLaughlin and Jih [36] observe a similar variation in waveforms from events at the French southern Sahara test site and show that the common dominant characteristics of P-coda for stations at similar take-off angles and azimuths may be attributed to direction-dependent scattering in the source region. The pP arrivals for these events show significant variability; for most stations and events there is no negative polarity pulse, while some waveforms suggest greatly delayed or multi-pathed pP pulses. Through 2-D numerical experiments McLaughlin and Jih [36] conclude that a rough surface topography may be responsible for these observations, causing wave scattering, focussing and defocussing.

A number of mechanisms are thought to influence the seismic wavefield in the near-source region, including: depth of burial, source magnitude, scattering off topography and structural heterogeneities, as well as non-linear effects. For explosions the latter includes tectonic strain release, cavity formation and collapse, and spall [45]. Moreover, non-linear changes in the properties of the near-source material can also lead to seismic radiation effects [5]. Since quantifying the contribution of non-linear interactions on the teleseismic waveforms is challenging, we focus on exploring the Degelen dataset for wavefield variations as a function of depth of burial, explosion magnitude and source location.

The spatial dependence (i.e., near-source signature) of waveform characteristics recorded at YKA is clearly demonstrated in Figure 3 (see Figures S1-S3 for the other arrays). Co-located events have near-identical recorded waveforms (e.g., events 12 and 46, or 90 and 99 in Figure 3), while moving the source location just a few kilometres results in visible differences. The first two seconds of the waveform are stable for events located in the same area, but it is within the coda that we see waveform variation. We observe both variation in the arrival time and in the amplitude of different waveform packets in the coda. Occa-
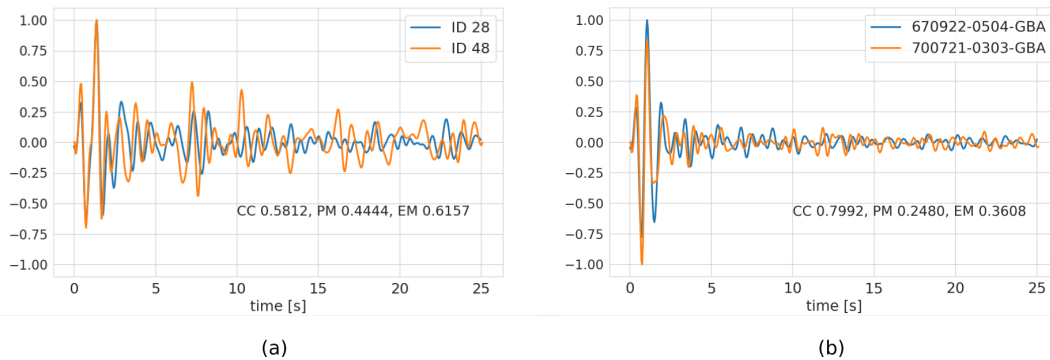
Figure 2: Examples of observed waveform differences for (a) Degelen and (b) Konystan events of similar depths recorded on GBA. The Degelen events in (a) were buried at 225 m (ID 28) and 219 m (ID 48) with $m_b$ of 5.58 (ID 28) and 5.26 (ID 48), respectively. The Konystan events in (b) were buried at 229 m (670922-0504) and 225 m (700721-0303), with $m_b$ of 5.22 and 5.39, respectively. All waveforms are normalised by the maximum amplitude, low-pass filtered at 2 Hz, and the P-wave onset is at $t = 0$ s. CC, PM and EM stand for cross-correlation, phase misfit and envelope misfit [25].

sionally the delay in energy is so large that an additional arrival becomes apparent (e.g., events 29 and 58, Figure 3), causing an effect resembling a cycle skip for the subsequent arrivals in the coda. In areas of high elevation even a small shift in source location can cause significant variations in the coda (e.g., events 42 and 67, Figure 3). On the other-hand, events that are located in significantly different parts of the mountain range (e.g., events 80 and 87, Figure 3 and S4b) can generate waveforms that have similar characteristics in certain time windows in the coda.

The degree of waveform variation differs between stations, with waveforms recorded at the closest array, GBA, displaying the highest complexity. However, the near-source signature is visible at all arrays as event location shifts along the ridges, with specific features progressively emerging and fading away as location changes. Given the spatial dependence of the waveform characteristics, clustering events by waveform shape could help elucidate the underlying near-source mechanism causing these observed differences. A previous study [41] attempted to cluster these events using a number of techniques, including waveform complexity measures [e.g., area under the envelope, Root Mean Square amplitude and weak-signal hypothesis, 14, 27], cross-correlation, as well as envelope and phase misfits [EM and PM, respectively, 25]. Unfortunately, determining a simple threshold for any of these metrics could not provide stable, spatial coherent clusters. In fact these metrics often average out the variations in a given time window (Figure S4) and hence mask the subtle signal characteristics observed in Figures 3 and S1-S3.

## 4 WAVEFORM CLUSTERING

### 4.1 Algorithms and Cluster Stability

We have tested two state-of-the-art approaches for shape-based clustering of time series implemented in the Python package tslearn [55]: a kernel k-means algorithm [13] with Global Alignment Kernel [GAK, 11], and a k-Shape algorithm based on normalised cross-correlations [38]. GAKs are not invari-

ant to time shifts, thus the k-means GAK-based clustering is not only shape dependent, but also phase dependent. With the kernel "trick" the cluster centroids are never computed explicitly, so the time series assignments to cluster are the only information available once the clustering is performed. The k-Shape approach, on the other hand, computes the centroids and is phase independent, clustering only by shape. This method introduces both a new cross-correlation-based distance metric as well as computations of cluster centroids specific to that new metric (that are then used for assignments), distinguishing it from the k-means algorithm.

To test the sensitivity of the output clusters we performed tests on a variety of time windows in the 0-20 s range and for waveforms low-pass filtered at 2 Hz, 4 Hz and 8 Hz. The algorithms also require the number of clusters to be pre-assigned (we tested 2-6 clusters), with the spatially-correlated optimal clusters robust and immediately distinguishable on all arrays. When we use a lower number of clusters we observe no spatial dependence of events, while using a higher number of clusters assigns low SNR waveforms to separate clusters with the dominant spatial pattern remaining (see Tables S2-S3 for details on clustering parametrisation and performance evaluation).

We obtain coherent and stable clustering results with both methods using just the first 5 s after the P-wave onset (Figure 4a and S5 for k-Shape and Figure S6 for GAK), where we observe the most prominent location-dependent features on all arrays. The k-Shape algorithm, using 0-20 s waveforms, also clustered events into nearly identical clusters to those using just 0-5 s waveforms (Figure 4b-e). GA kernel-based classification problems have proven to be more stable for short time-series of < 100 time samples, with the GA kernel values tending to infinity for longer time series [4]. In our clustering problem, the 0-5 s window has exactly 100 time samples and also showed the best performance: the time window includes enough information to cluster the waveforms, and yet is short enough for the GAK-based kernel k-means algorithm to remain stable. Despite the stability issues, successfully employing GAK for the 0-5 s window validates the k-Shape clusters and demonstrates
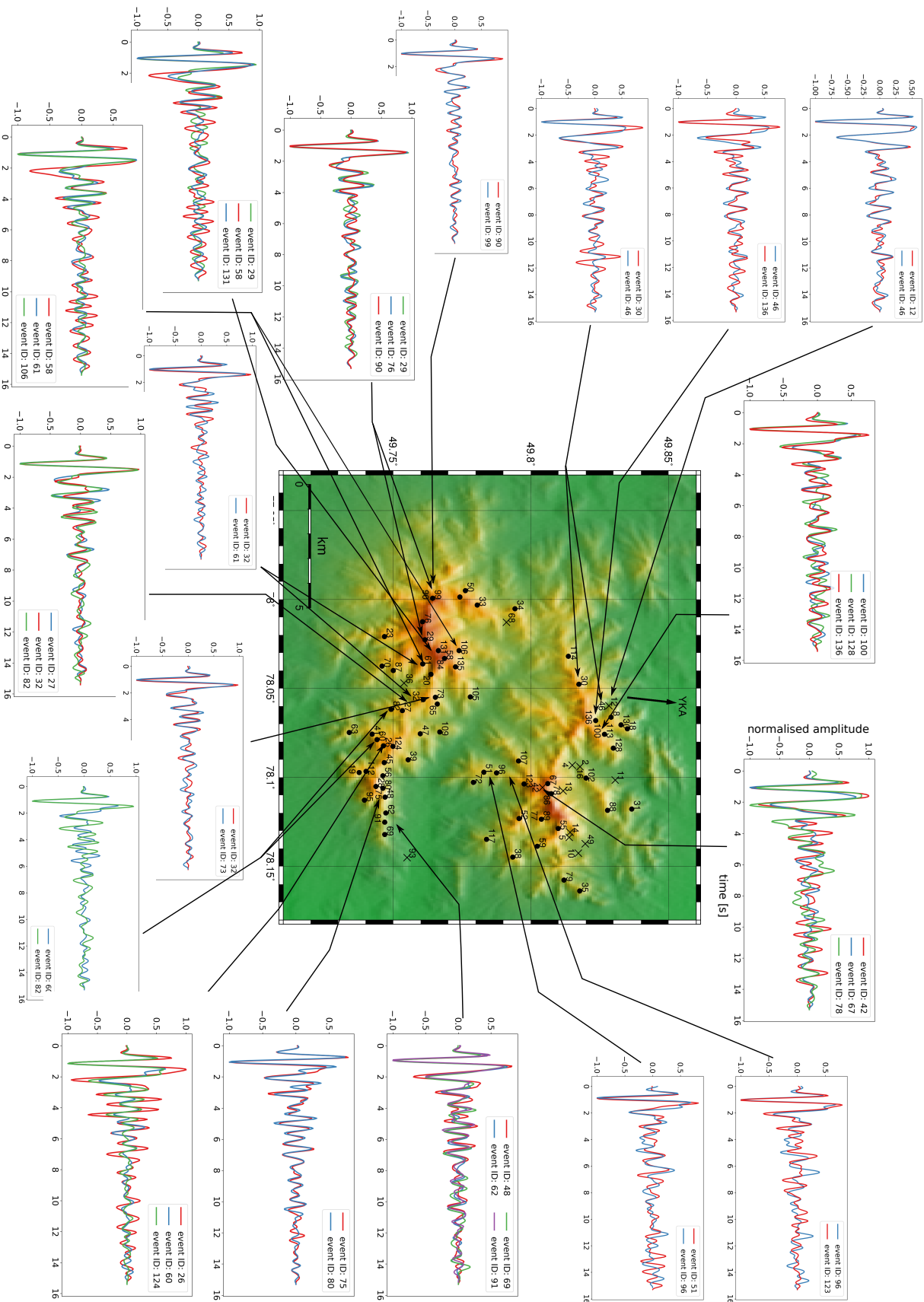
Figure 3: Degelen events recorded at YKA. All waveforms have been low-pass filtered at 2 Hz. The direction to YKA is indicated with an arrow. Events at known adit ends [56] are represented by circles. Events without known adit-end locations, are plotted as crosses at the GPS-determined locations of adit entrances [30]. For better clarity the waveforms have been cut at 15 s.

that the results are robust and based on information in the waveforms.

A full Silhouette analysis [47], with Silhouette Coefficients for each sample, is shown in Figure 5 for the k-Shape clustering of the 0-20s time windows low-pass filtered at 4 Hz. A Silhouette Coefficient for a given sample is computed using the mean intra-cluster distance and the mean nearest-cluster distance. The Silhouette plot for all samples shows how close a waveform in a given cluster is to waveforms in the neighbouring clusters. Coefficients close to 1 indicate that the given waveform is "far" from the neighbouring clusters, that is, it is considered to be well assigned. A value of 0 indicates some uncertainty, namely that the waveform is close to the decision boundary between two neighbouring clusters. Negative values indicate that those waveforms might have been assigned to the wrong cluster.

Overall, the plot confirms the stability of the obtained clusters. All Silhouette values are small, below 0.5, which is expected given the high similarity of the observed waveforms for each array. Notably, the values are higher for GBA and YKA (where the clusters have proven to be more stable) and lower for EKA and WRA (where higher frequency information was required for cluster stability). Unsurprisingly, we see a small degree of ambiguity regarding the assignment of the waveforms to clusters – as the observed change of waveforms is progressive on each array, such behaviour is expected. The Silhouette plot confirms the challenge of strictly delineating where one cluster ends and the other begins, although the number of negative silhouette values is small. The mean Silhouette Coefficient [47], the Calinski-Harabasz Index [8] and the Davies-Bouldin Index [12] complement the silhouette analysis and show that the separation of clusters is lower for 2 Hz k-Shape clusters and higher for 4 Hz (Table S2).

## 4.2 Frequency Dependence

The assignment of waveforms to clusters appears to be influenced by the frequency content of the waveforms. The k-Shape determined clusters using 20 s waveforms from YKA and GBA show minimal changes when waveforms are low-pass filtered at 2 Hz or 4 Hz (Figure 4b and 4e). The WRA 2 Hz low-pass filtered waveforms form three distinct groups, but the assignment is less stable, varying with window length (Figure 4a vs. 4b). This improves for waveforms low-pass filtered at 4 Hz, suggesting some frequency dependence. This frequency dependence is even more striking for waveforms observed at EKA. EKA waveforms filtered at 2 Hz are assigned to two spatially distinguishable clusters. Using EKA waveforms filtered at 4 Hz, a clear stable three-cluster pattern emerges with a similar spatial distribution as seen at the other arrays.

Spectra (Figure S7) for each of the waveforms help shed some light on this observation: the relative importance of the energy in the 2-4 Hz range is higher for EKA and WRA than for GBA. Interestingly, the YKA signal in the 2-4 Hz range, although comparable in relative amplitude to EKA, does not help to refine the clustering. It must be noted that we use limited bandwidths beams and the beamforming process itself acts as a low-pass filter. Since the waveforms do not contain much energy

above 4 Hz, frequencies in the 4-8 Hz range did not change the clustering results.

The clustering performance metrics (Figure 5, Table S3 and Text S2) indicate that GBA has the highest separation of clusters, while EKA the lowest. The metrics for GBA, YKA and WRA improve for the 4 Hz clusters relative to the 2 Hz clusters, in particular supporting the observed increased stability of the 4 Hz clusters at WRA. Comparing the EKA metrics, however, is not meaningful, as the number of clusters changes using a different frequency band.

## 4.3 Azimuthal Dependence

The cluster assignment is not identical for all arrays, suggesting some azimuthal dependence to the propagation of the near-source effects, but the overall pattern remains similar. The events in the south-west (cluster 2, orange) emerge as a distinct group on all arrays and are the most coherent group between the arrays. The events in the south-east (cluster 3, green) and in the north (cluster 1, blue) also are identified on all arrays, with two notable differences. On GBA the northern ridge is separated into two clusters, with an additional group of events emerging towards the centre (cluster 4, red). On YKA all events on the east side belong to one cluster (cluster 3, green), with the north-east events more similar to the south-east rather than the north-west (cluster 1, blue) like on the other arrays.

This directionality also appears to be related to the frequency content of the waveforms. For the stations with azimuths to the north and south, perpendicular to the valley separating the ridges (GBA and YKA), the 2 Hz waveforms lead to successful, stable cluster assignments. Stations with azimuths to the north-west and south-east, parallel to the valley separating the ridges (EKA and WRA) require waveforms with frequencies up to 4 Hz for the clear spatial pattern to emerge. Cluster 2 in the south-west, however, is not influenced by this directionality related to the frequency content. The events in the south-west can be identified on all arrays using waveforms that are low-pass filtered at either 2 or 4 Hz, indicating that the underlying mechanism in this area generates waveform features that are dominated by frequencies of 2 Hz.

## 4.4 Time Window Length Dependence

It has previously been observed that the first 5 seconds of explosion seismograms are the most coherent and visibly change with location, while the later coda tends to exhibit less coherence [e.g., 14, 27]. Our clustering results using 0-5 s time windows further demonstrates that such a short time window carries enough information for the spatial pattern to emerge. However, the k-Shape clusters are more stable and consistent for the 0-20 s window compared for the 0-5 s window (Figure 4a vs 4b, in particular for EKA and WRA arrays), suggesting that some coherent features after the first 5 s carry the near-source signature. A clustering analysis of the coda in the 5-20 s window, however, suggests that the later-arriving energy overall carries less information about the event locations. In the case of GBA, EKA and WRA nearby events did not get grouped together. For the clustering of YKA 5-20 s coda, however, we observe stable three clusters corresponding to those in Figure 4 (see Figure S8).
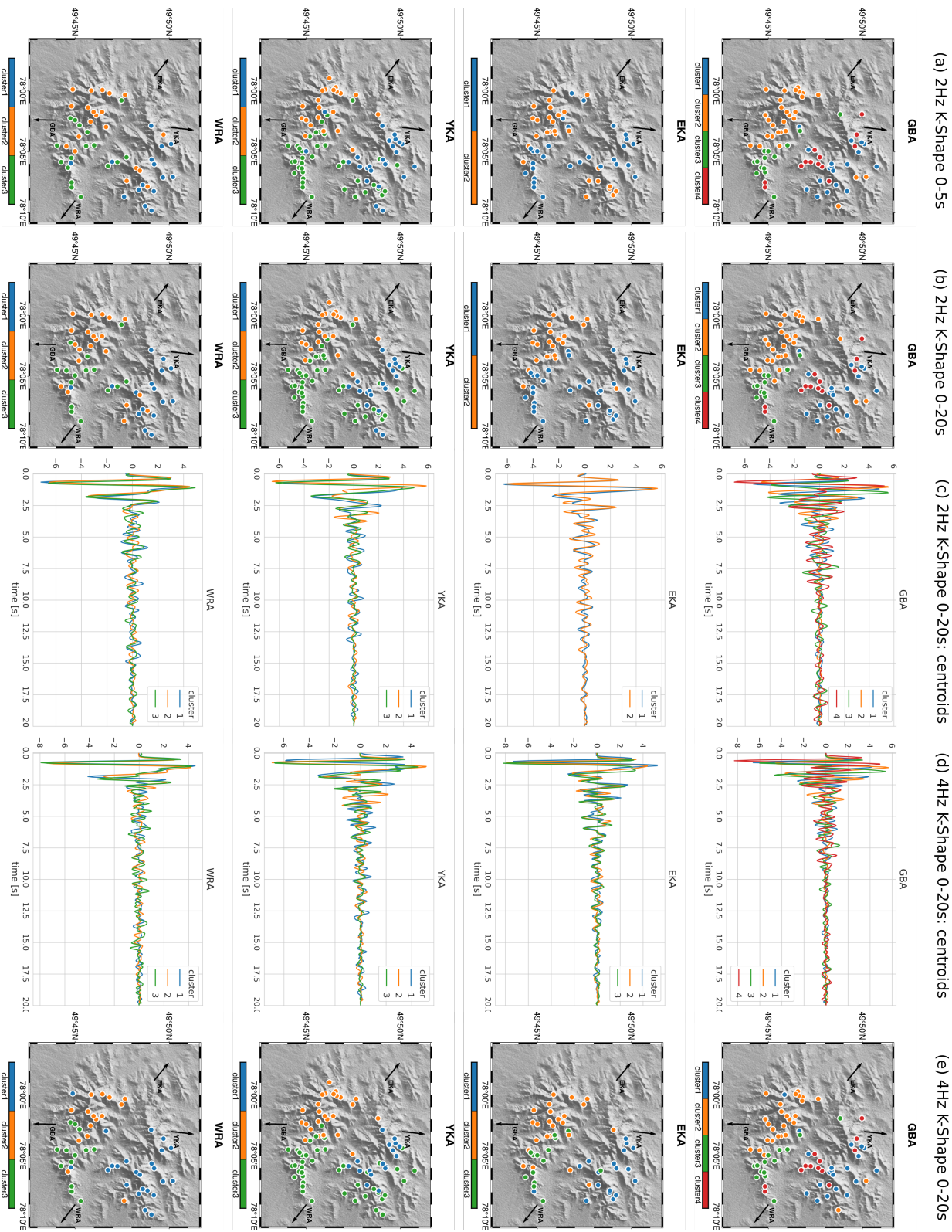
Figure 4: Clustering results for the k-Shape algorithm. The clusters are shown for waveforms low-pass filtered at 2 Hz for the (a) 0-5 s and (b) 0-20 s time windows. The corresponding cluster centroids for the 0-20 s time window for waveforms low-pass filtered at 4 Hz. Note that the values on the y-axis in (c) and (d) are the result of the z-normalisation by the standard deviation of the amplitudes, the method of choice for the k-Shape algorithm [38].
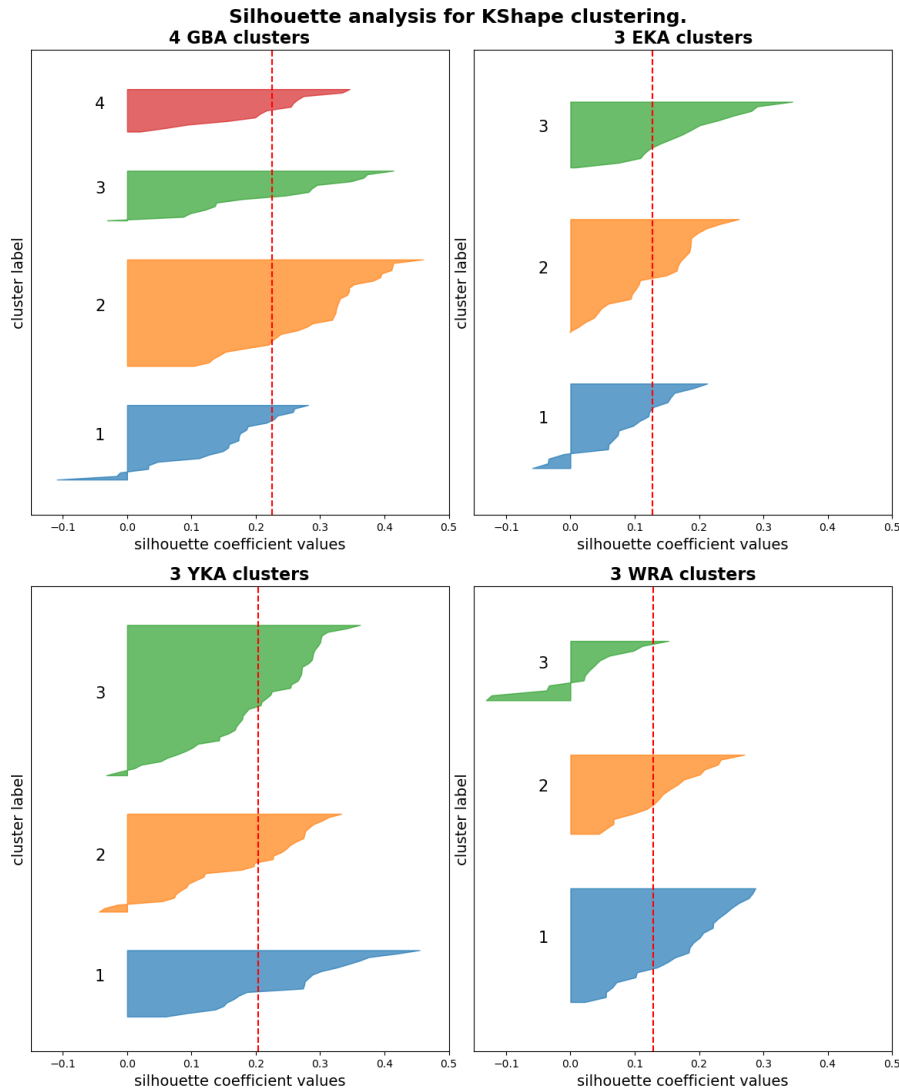
Figure 5: The Silhouette analysis of the k-Shape clusters obtained for 20 second waveforms filtered up to 4 Hz, with the value of the Silhouette Coefficient for each event on the x-axis. On the y-axis, each event is plotted within its assigned cluster and events within each cluster are sorted according to the values of their silhouette coefficients in the decreasing order (top to bottom). The vertical red line indicates the average Silhouette score for all values (see Table S3). The value of the Silhouette Coefficient ranges between -1 and 1, with 1 indicating good assignment. Negative values suggest that the sample may have been assigned to the wrong cluster. Values close to zero indicate some ambiguity, meaning that they are close to the cluster boundary. The plot highlights the difficulty of strictly delineating the clusters, as the waveforms change progressively for sources along the ridges.

## 5 CLUSTER INTERPRETATION

Whatever near-source mechanism is generating these waveform variations, we can observe its signature on all stations, albeit to a different degree: as can be expected, the effect is direction- and frequency-dependent. An appropriate source model [37] representative of the Degelen explosions (a 15 kT explosion at 170 m depth in granite) has a seismic moment of approximately $10^{16}$ Nm and a corner frequency of 1.5 Hz. The energy up to 2 Hz therefore dominates the seismograms (see Figure S7), with clusters capturing the near-source interactions of the wavefield. Waveforms at stations with azimuths to the north and south (YKA and GBA), perpendicular to the valley, cluster into two stable, spatially distinct groups at frequencies of $\leq 2$ Hz. Frequencies above 2 Hz are visible in the waveforms, but neither improve the existing clusters nor do they allow the identification of finer clusters. The coda in the 2-4 Hz range, on the other hand, proves crucial to improving the clustering for the waveforms at stations with azimuths to the north-west to south-east (EKA and WRA) parallel to the valley.

To interpret the clusters, in the following we first consider event depths and magnitudes, as well as nonlinear effects such as spall and tectonic release, as possible sources of waveform variation. We then focus on the Degelen topography and perform both local and teleseismic simulations in 3-D to understand how it affects the wavefield.

### 5.1 Comparison of cluster locations with event depth, magnitude and tectonic release

Due to containment, the depth at which a nuclear explosion is detonated is generally related to the yield: the larger the explosion the deeper the shot point. An initial examination of the waveforms suggests that depth and $m_b$ are not the primary factor effecting the shape of the waveforms. Events with the same depth and thus comparable $m_b$ (e.g., event 31 at 160 m depth with an estimated $m_b = 5.40$ and event 32 at 161 m depth with an estimated $m_b = 5.34$, 10 km apart, Figure 3) produce significantly different waveforms on all arrays, while events with different burial depths and thus different $m_b$ (e.g., event 26 at 241 m depth with an estimated $m_b = 6.08$ and event 41 at 162 m depth with an estimated $m_b = 5.47$, 500 m apart, Figure 3) that are located in close proximity can generate nearly identical coda waves [41]. Comparing event depth, $m_b$, and the k-Shape determined clusters we find no spatial relationship linking event location (waveform shape) with either event depth or event $m_b$ (Figure 6a), thereby confirming the initial analysis that neither event depth nor $m_b$ are the dominant factors influencing the teleseismic waveforms for the Degelen events observed at EKA, GBA, YKA and WRA.

Spall, the process of detachment and slapdown of near-surface material above an explosion due to induced tensile stresses, is commonly observed for underground nuclear tests. Schlittenhardt [49] demonstrates using theoretical seismograms that spall can significantly alter teleseismic body waves. In particular, spall increases the peak-to-peak amplitudes and can increase the higher frequencies compared to synthetics calculated without spall. Simulations reveal that effect of spall on the seismic wavefield is complicated and depends critically on the kinematic spall characteristics such as spall dwell- and rise-

time [49]. Given the consistency of the waveforms seen across the Degelen test site, even though there is variation in depth and magnitude of the events, it is unlikely that spall is having a significant influence on the observed teleseismic waveform shapes. Since the spall dwell-times predicted for event depths at Degelen are small, it is likely that spall would only effect the first 1 s of the observed seismic waveforms and would not be the source of coda variation we observe.

Rygg [48] suggested that tectonic prestress can effect explosion-generated surface waves, but the effect of a 3-D prestress field on far-field body waves had not been previously investigated. Stevens and Thompson [52] compare calculations with observations of the Shoal nuclear explosion: the simulations are consistent with near-field and regional signals, including long-period surface waves. They demonstrate that tectonic release causes small changes to the far-field P-wave waveform but has very little effect on far-field P-wave amplitudes, and suggest non-linear effects above the explosion have a much stronger effect on body waves than tectonic release.

Without additional detailed information, we can not link the variation in waveform shape to factors within the near-source non-linear regime and those are therefore not considered further in this study. As the Degelen test site sits on a relatively homogeneous granite massif, we do not expect these waveform variations to result from near-source structural heterogeneities, and thus we choose to focus on the surface topography for the remainder of this study.

### 5.2 Comparison of cluster locations with near-source topography: 3-D local simulations

It is well known that the interaction of the wavefield with topography can cause variations in waveforms, but can the topography at Degelen explain the event clusters we observe? Amatulli et al. [2] use global digital elevation models to derive a suite of global, cross-scale topographic variables (e.g., elevation, slope, terrain roughness index, topographic position index). The derived topographic variables were calculated based on the value at each grid cell individually, or a set of grid cells in the immediate vicinity of each particular cell as defined by a $3 \times 3$ moving window (i.e., a particular focal cell with eight surrounding cells). We compared numerous of these topographic variables with the cluster assignment for each array (e.g., Figure 6b-c). However, we could not identify any one topographic property that correlated with the spatial distributions of the clusters. Since the events in one single cluster have different depths and are distributed over an area of a few kilometres, their positioning relative to the slopes in their immediate vicinity varies. It suggests that the waveform variations are generated by reverberations from a section of the mountain range with specific topographic characteristic length scales, rather than the particular topographic irregularity under which the event took place.

In order to test this, we perform local simulations of isotropic explosions in the Degelen massif. We implement the 90 m Degelen topography from NASA's Shuttle Radar Topography Mission [SRTM, 16] within the 3-D Wave Propagation Program [WPP, 40]. Since the flat steppe surrounding the Degelen peaks has elevations of about 500-600 m above sea-level (see profiles in Figure 1), defining the local simulation domain to en-
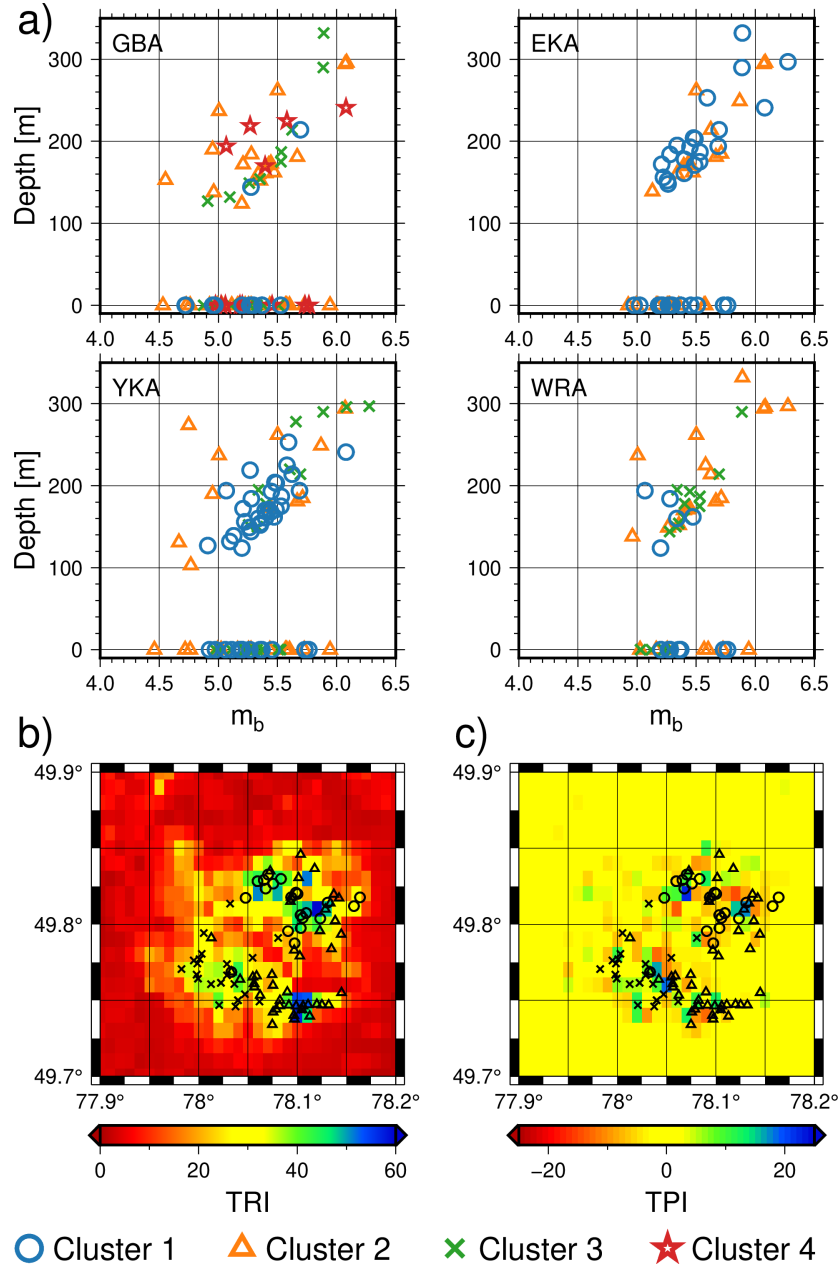
Figure 6: Event clusters with respect to (a) depth and body wave magnitude ($m_b$), where zero depth indicates that the corresponding depth has not been published, (b) the Terrain Ruggedness Index [TRI, 2], (c) the Topographic Position Index [TPI, 2]. There is no relationship between the clusters and event depths, moment magnitudes, or specific topgraphic properties.
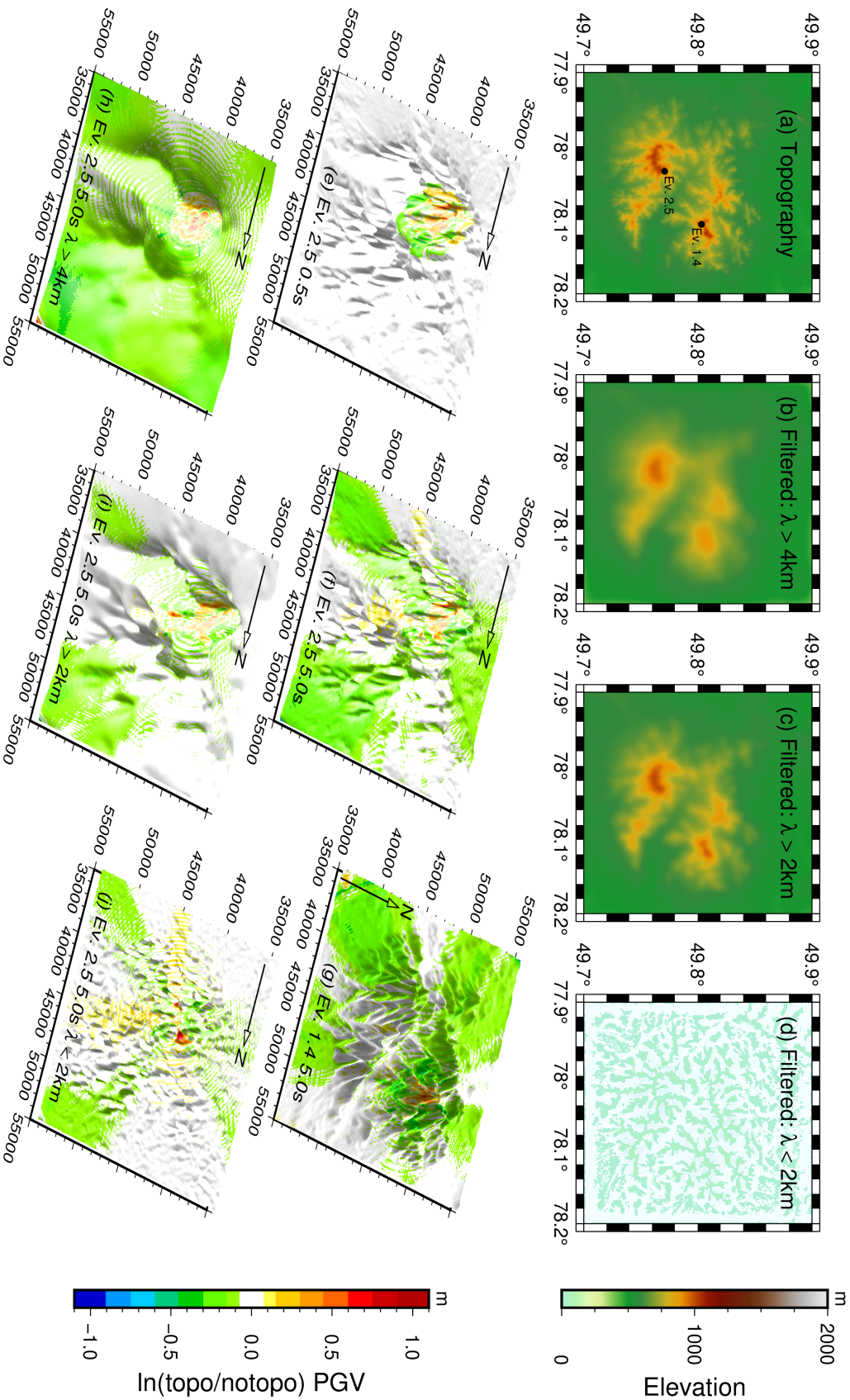
Figure 7: Effect of surface topography on Peak Ground Velocity (PGV) for local simulations [using WPP, 40]. In the top panels, the SRTM topography at the Degelen test site filtered for different wavelengths: (a) no filtering, (b) only wavelengths > 4 km, (c) only wavelengths > 2 km, and (d) only wavelengths < 2km. In the middle and bottom panels PGV ratio plots for two synthetic explosions located in the south-west (event 2.5) and north-east (event 1.4), with locations indicated in (a). In particular, in the middle panels, the PGV ratio plots for the unfiltered topography for an explosion located in the south-west, event 2.5, (e) 0.5 s and (f) 5 s after the detonation, as well as (g) for an explosion located in the north-east, event 1.4, 5 s after the detonation. In the bottom panel, the PGV ratio plots for an explosion located in the south-west, event 2.5, 5 s after the detonation, using (h) topography with only wavelengths > 4 km, (i) topography with only wavelengths > 2 km, and (j) topography with only wavelengths < 2km. We plot the natural logarithm PGV ratio for simulations with topography (topo) and simulations which are flat (notopo). This quantifies the effects of surface topography and shows that motions are amplified or trapped on peaks and along ridges, close to the detonation point, even 5 s after the detonation. Note that the panels for simulations in the south-west (for event 2.5) are rotated for better visualisation.

compass only the sharp topography of interest results in model boundaries at an elevation of 500-600 m. In our case, however, the local simulations are subsequently used for injecting wavefields into a global wave solver, which requires the edges of the local 3-D domain to match the zero elevation of the spherically symmetric Earth (see next subsection). Given that we aim to isolate the influence of only the sharp topographic features, we remove both the surrounding elevation and the underlying topographic trend (Figure S9a,b). Similarly, the background 1-D velocity model of the local WPP simulations is required to match the global model that is subsequently used for teleseismic propagation (Figure S9c). Given the velocity structure under Degelen [1], we select IASP91 [23] for our purpose, so that velocities in WPP simulations match the top layer of IASP91.

To isolate the effect of surface topography on the seismic wavefield we plot (Figure 7e-g) the natural logarithm ratio of the Peak ground velocity (PGV) for a local simulation with flat topography (notopo) with a local simulation including topography (topo) for two sources across the Degelen mountain range. The simulations confirm that the seismic wavefield is not influenced by a single peak but by the reverberation of multiple peaks (amplitude motions) surrounding the source region, and indicate that the location where they are triggered is crucial. Comparing synthetic explosions in the southern and in the northern ridge shows that the location of the explosion determines the "ringing" of a particular section of the mountain range and the corresponding release of energy (Figure 7f vs. 7g for southern and northern ridge, respectively, for 5 s after the detonation). The location both defines where the energy remains trapped, with reverberations directly above the source, as well as how and when the more distant peaks in the mountain range are excited. We thus postulate that it is this overall superposition pattern of the energy leaving the reverberating peaks that results in the teleseismic waveform differences and explains the progressive change in waveform features illustrated in Figure 3. As we shift the location, we modify the "ringing" and the timing of the arrival of the multiply scattered phases changes progressively.

As suggested by Marshall et al. [35] the waveform clustering demonstrated a frequency-dependent directionality, indicating that the release of the reverberating energy is direction dependent. Rodgers et al. [46] showed with local numerical simulations of the Democratic People's Republic of Korea (DPRK) nuclear explosions that topography with scale lengths of less than 5 km alters the seismic response in a strongly path-dependent manner. Azimuths with smoothest topography show the weakest amplification of the P-wave coda energy, in particular above 2 Hz, while the azimuths crossing ridges and rougher topography show the highest amplifications. At Degelen, the north-west to south-east topographic profiles (Figure 1, profiles A and B towards EKA and WRA) have more pronounced features on the scale of 1-2.5 km (P-wave frequencies of about 2-5 Hz). The north-south topographic profiles (Figure 1, profiles C, D and E towards YKA and GBA), on the other hand, are dominated by features on the scale of 2-4 km (P-wave frequencies of about 1.3-2.5 Hz). Although such 2-D profiles do not fully represent the complex 3-D response of the massif, they indicate why clustering was effective at YKA and GBA for waveforms filtered at 2 Hz.

The topographic length scales also explain why the events in the south-west (cluster 2, orange) can be clearly identified on all arrays using waveforms low-pass filtered at 2 Hz. As shown in Figure 7b-c, filtering the Degelen topography for wavelengths > 2 km or > 4 km reveals 3-4 distinct sections of the mountain range that are spatially similar to the clusters shown in Figure 4: two distinct clusters on the southern ridge and a more complex picture to the north. To understand the sensitivity of the reverberations to different topographic wavelengths we re-run the local simulations with filtered topography (Figure 7h-j, corresponding to the unfiltered simulation in Figure 7f, 5 s after the detonation). The resonance can be observed on the local synthetic wavefield even with the long-wavelength filtered topography (Figure 7h), albeit without the smaller-scale complex reverberations of the unfiltered topography. In particular, the area in the south-west is dominated by topography with a characteristic length scale of 2-4 km, corresponding to 2 Hz resonance. This strong resonance at 2 Hz affects the wavefield in all propagation directions to such a degree that the corresponding cluster could be identified on all arrays for 2 Hz waveforms.

Our findings for the Degelen data support the conclusion of Rodgers et al. [46] that the interaction between the azimuthal direction to the station with the near-source topography plays a role in the scattering efficiency in a given direction. In particular, we can observe such local effects in the Degelen waveforms at teleseismic distances, and our local simulations suggest that the alignment of the characteristic scale lengths is behind the identified frequency-dependent directionality.

### 5.3 Comparison of cluster locations with near-source topography: Teleseismic simulations

Stevens and O'Brien [51] performed local non-linear simulations of DPRK explosions that they extrapolated to teleseismic distances using the representation theorem. In particular, the non-linear simulations incorporate gravity and thus the effects resulting from variation of overburden pressure with depth. They reported a strong variation of amplification with azimuth, especially of the pP phase, as well as yield-dependence. The focusing and defocusing was significantly reduced for a 180 kT event relative to a 20 kT event because of the increased non-linear interaction of the larger explosion with the free surface. Although at Degelen the yields do vary (most events were 4-20 kT with only a small number between 20-125 kT), the teleseismic waveform variations appear to be dominated by the location relative to the topography rather than by yield.

In order to capture the propagation of the scattering off the Degelen topography to teleseismic distances, we employ an injection- and extrapolation-type hybrid framework proposed by Pienkowska et al. [42]. The framework couples wavefields from a precomputed global database of accurate Green's functions for 1-D models [Instaseis, 57] with local 3-D simulations, allowing us to embed a 3-D domain in a spherically symmetric Earth model. In particular, the method was successfully benchmarked for source-side coupling with WPP: when the local 3-D domain in WPP implements the 1-D global model from the database, the hybrid method exactly reproduces the 1-D seismograms [42].

**(a) locations of synthetic events**



**(b) synthetic seismograms for all events**



**(c) synthetics vs data**
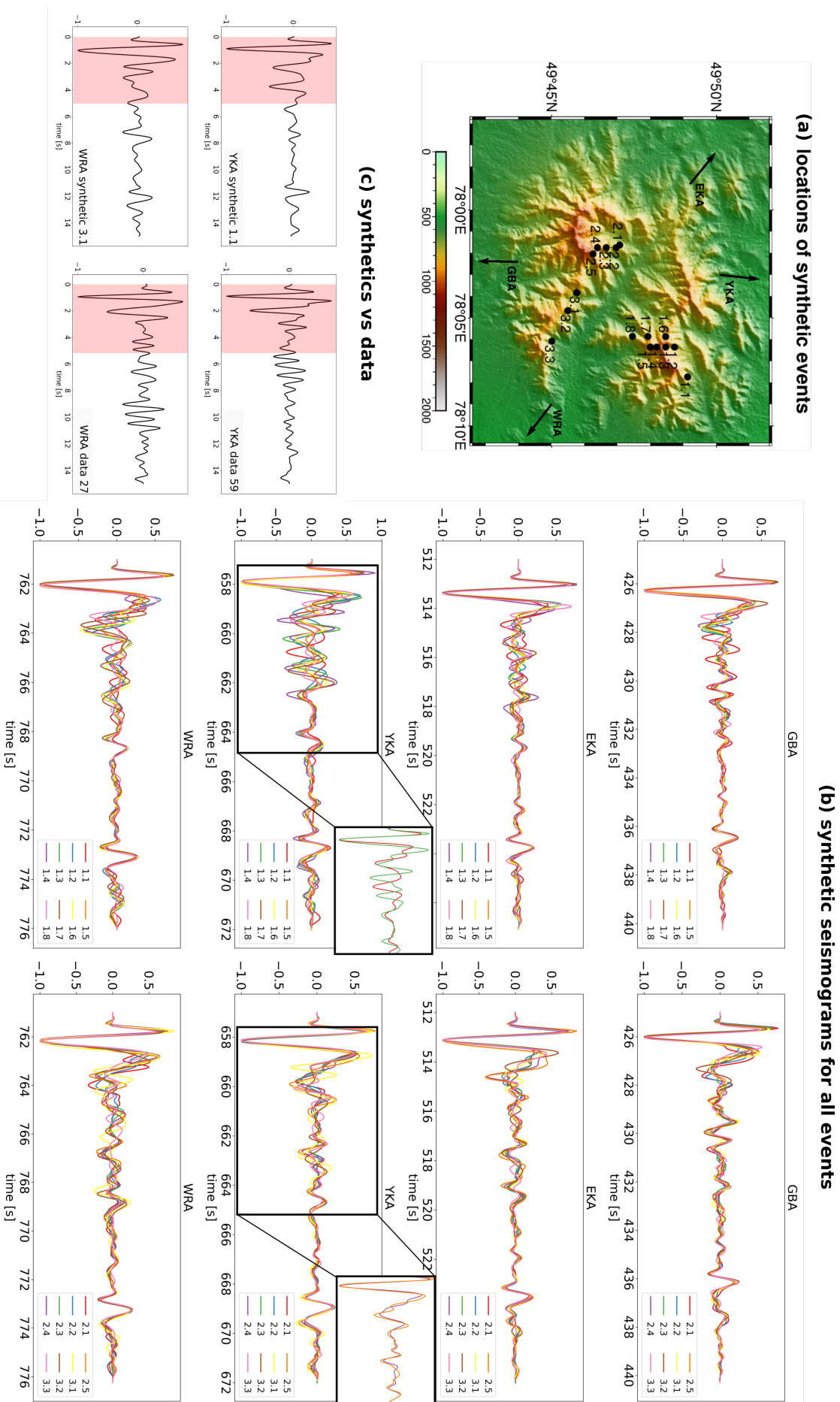


Figure 8: (a) Locations of the sixteen synthetic explosions simulated with the hybrid method along with (b) the corresponding seismograms at GBA, EKA, YKA and WRA and (c) a comparison with real data for selected events at YKA and WRA. Eight events were simulated on the northern ridge (1.1-1.8 located in the area of cluster 1,) and eight events on the southern ridge (2.1-2.5 located in the area of cluster 2, and 3.1-3.3 located in the area of cluster 3). The resulting synthetic waveforms are strongly affected by the Degelen topography on all arrays and reproduce some waveform characteristics visible in the data.

We generated an IASP91 [23] Instaseis database with a maximum frequency of 2 Hz (corner frequency of 1 Hz). The local region of $30 \times 30 \times 10$ km that includes the 'tapered' topography (see section above and Figure S9a,b) is embedded in the global IASP91 model. The local domain remains above the 20 km discontinuity of the IASP91 model and therefore the local background velocity model is homogeneous (Figure S9c). It should be noted that by including only the peaks of the Degelen mountain complex we marginally change the angle of the slopes relative to the source-receiver paths.

We simulated eight events on the northern ridge (1.1-1.8 located in the area of cluster 1) and eight events on the southern ridge (2.1-2.5 located in the area of cluster 2, and 3.1-3.3 located in the area of cluster 3; Figure 8a). Synthetic seismograms for all sixteen locations at GBA, EKA, YKA and WRA are shown in Figure 8b, illustrating that we reproduce similar effects to those observed in the data. The teleseismic synthetics isolate the topographic effect and show that variations in the amplitudes and arrival times of different waveform packets in the coda are related to the reverberating peaks. Like in the real data the delay in energy can be so large that additional arrivals become apparent (for example YKA 1.1 and 1.3 highlighted in Figure 8b), while events close by remain very similar (for example YKA 2.4 and 2.5 highlighted in Figure 8b). Moreover, similarly to real data, the first 5 seconds of the seismograms visibly change with location, but the effect of the topography is also visible in all of the later arriving coda. In particular, some distinct waveform characteristics can be reproduced and associated with the topography, like the splitting of the second peak that we observe on all arrays both in the data and in the synthetics (e.g. Figure 8c for YKA).

Given the simple modelling assumptions and the corner frequency of only 1 Hz, the simulated waveforms are less complex than the real data on all stations. The dependence of the complexity on take-off angle and azimuth is lower in the synthetics, in particular for the GBA array with the most complex of the recorded waveforms. Overall, the teleseismic synthetics compare much better to the observed waveforms at EKA, WRA and YKA. We do not reproduce the complicated seismograms at GBA, likely missing some crucial 3-D effect that is not captured in our spherically symmetric velocity model. Moreover, the prominent 20 km and Moho reflections at 7 and 11 seconds after the onset in the synthetics, respectively, are generally less discernible in the data. This is to be expected, as discontinuities in the real Earth are not at a constant depth, and the source-receiver symmetry with respect to the 1-D discontinuities is broken.

Despite these differences we use the YKA 2 Hz k-Shape model for the 0-20 s time window to predict which clusters each of the synthetic waveforms for YKA belong to (Figure 9). Events 3.1–3.3 in the south-east are all correctly predicted to belong to cluster 3. Events 2.1–2.4 in the south-west again are correctly predicted to belong to cluster 2, but event 2.5 is incorrectly assigned to cluster 1. Event 2.5 is actually close to the boundary of cluster 1. We should note that waveforms for events 2.4 and 2.5 are in fact very similar (as highlighted in Figure 8b), yet some subtle difference leads the algorithm to assign them differently. Events 1.1–1.6 in the north-east are correctly assigned to cluster 1, but events 1.7 and 1.8 are assigned to cluster 2.
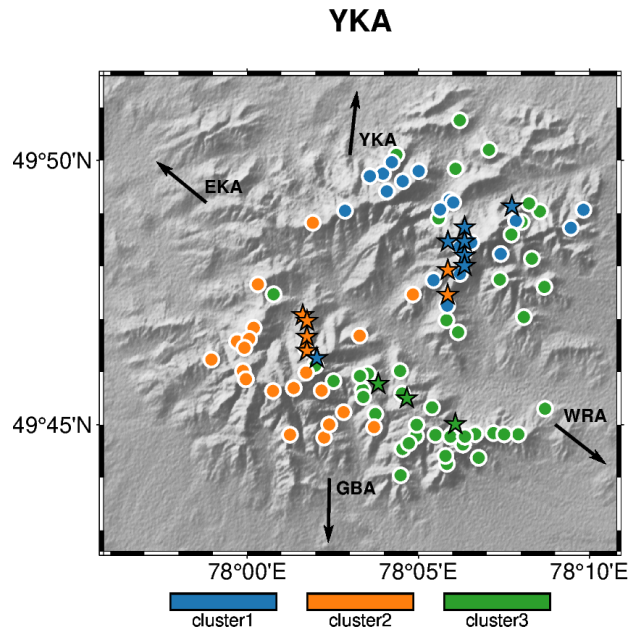


Figure 9: The prediction of the closest cluster for the YKA synthetic waveforms with the 2 Hz k-Shape model for the 0-20 s time window. Circles represent the real YKA explosions used to generate the model for the 2 Hz clusters, while stars represent the locations of the synthetic events. The correct assignments indicate that relevant waveform characteristics picked up by the clustering algorithm are related to the Degelen topography.

Again, these events sit in a boundary region. Given the generally low separation between the clusters there is some ambiguity even in the data, so we do not expect to accurately predict all waveforms – in particular, the misclassified events are close to cluster boundaries, where such behaviour can be expected. The overall correct assignments of the synthetic waveforms at YKA, however, are a further indication that relevant waveform characteristics picked up by the clustering algorithm are related to the surface topography at Degelen and its effect on the seismic wavefield. Note also that for 2 Hz the YKA model is the only possible testbed for such predictions. The 2 Hz WRA and EKA models are significantly less robust and higher frequency content was needed for correct cluster separation. Although the 2 Hz GBA model was stable, the GBA synthetics do not reproduce the observed waveform complexity. As previously mentioned, this likely due to a take-off angle and azimuth related 3-D effect that is not fully captured in the spherically symmetric approximation.

## 6 CONCLUSIONS

We have revisited digitised data from underground nuclear explosions at the Degelen test site to examine the dependence of waveform features on the near-source region. An initial visual analysis, showing a progressive variation in waveform shape with specific features emerging and disappearing as event location changes, has been confirmed by a clustering analysis which revealed spatially distinct event groups for all arrays. A different degree of waveform complexity is observed between the

arrays and yet similar event clusters could be identified. Given the high waveform similarities (e.g., 2 Hz EKA centroids, Figure 4c), it is remarkable that a spatial pattern of robust clusters emerges.

Knowledge of the event depths and sizes allows us to eliminate these parameters as the source of the spatially distinct clusters. Local waveform simulations highlight that the seismic wavefield is not influenced by a single topographic peak above the source, but by the reverberation of multiple peaks surrounding the source location. At the Degelen test site it appears that topography with characteristic wavelengths of 2 - 4 km dominates the wavefield reverberations in the near-source region. The location of the explosion is crucial in determining which section of the mountain range reverberates that influences the outgoing wavefield. Teleseismic waveform simulations confirm that it is this superposition of energy leaving the reverberating peaks that results in the observed teleseismic waveform difference we observe at EKA, GBA, WRA and YKA. In particular, our results highlight that full 3-D wavefields are essential to capturing and understanding such complex and highly frequency-dependent effects.

Although the clustering helped us to delineate some of the distinct features and the established clusters are stable, it should be noted that there was some ambiguity in the assignment of waveforms to clusters. The observed change of waveforms is progressive on each array, and one ought to be cautious to not over-generalise the complex topographic effects. Waveforms even within each cluster can vary significantly, as they are sensitive to a particular effective topography over the entire mountain range, although some common characteristics are picked out by the clustering algorithms that group the waveforms together. Some events that are located in significantly different parts of the mountain range share waveform characteristics and get allocated to the same cluster, while events that are in close spatial proximity are allocated into two separate clusters. This indicates that the effective topography is important and is far from equivalent to a simple smoothed version used in the simulations. Although filtering the topographic undulations helps us shed some light on the reverberations, it is a coarse simplification of the effective topography at a given frequency that affects the waveforms observed at Degelen – there might be longer-wavelength characteristic regimes that significantly contribute or dominate these effects, beyond reverberations of individual peaks and valleys [see also homogenisation for finding effective behaviours, e.g., 9].

Other clustering algorithms [e.g. hierarchical clustering, 50] or waveform complexity measures [e.g. multiscale entropy, 15] could be tested to further our understanding of how surface topography may influence seismic wavefields and in particular of the effective topographic behaviour in different frequency regimes. The modelling framework could also be extended in an attempt to better reproduce the observations and thus to better understand the contribution of topography to waveform complexity, for example through including higher frequencies, accounting for the effects of yields (and the corresponding moment rate functions) and non-linear interactions, as well as including finer-resolution topography, near-source heterogeneities or more complex path and receiver effects [e.g., AxiSEM3D, 31].

Insights from an analysis of wavefields generated by nuclear explosions can guide future studies in earthquake seismology. Seismically active regions are often highly heterogeneous, with strong topography and complex structures surrounding the rupturing fault, while most methods to constrain earthquakes and the Earth's structure usually start from 1-D PREM-like models. Moreover, a trade-off between near-source interactions and the pure source radiation suggests that complex heterogeneities can influence the moment-tensor solutions and earthquake locations.

The file has been compiled with the latex template provided by https://github.com/brenhinkeller/preprint-template.tex.

## REFERENCES

[1] V. Adushkin and A. Spivak. Underground explosions. Unlimited DOS Contract No. SAQMMA13M2475, Air Force Technical Applications Center Directorate of Nuclear Treaty Monitoring (HQ AFTAC/TT), Patrick Air Force Base, FL 32925, 2015.

[2] G. Amatulli, S. Domisch, M.-N. Tuanmu, B. Parmentier, A. Ranipeta, J. Malczyk, and W. Jetz. A suite of global, cross-scale topographic variables for environmental and biodiversity modeling. *Sci. Data*, 5(1):180040, 2018. ISSN 2052-4463. doi: 10.1038/sdata.2018.40.

[3] D. Asimaki and K. Mohammadi. On the complexity of seismic waves trapped in irregular topographies. *Soil Dyn. Earthq. Eng.*, 114:424–437, 2018. ISSN 0267-7261. doi: 10.1016/j.soildyn.2018.07.020.

[4] M. Badiane, M. O'Reilly, and P. Cunningham. Kernel Methods for Time Series Classification and Regression. In *Proceedings for the 26th AIAI Irish Conference on Artificial Intelligence and Cognitive Science*, Trinity College Dublin, Dublin, Ireland, 2018.

[5] Y. Ben-Zion and J.-P. Ampuero. Seismic radiation from regions sustaining material damage. *Geophys. J. Int.*, 178 (3):1351–1356, 2009. ISSN 0956-540X. doi: 10.1111/j. 1365-246X.2009.04285.x.

[6] V. S. Bocharov, S. A. Zelentsov, and V. N. Mikhajlov. Characteristics of the 96 underground nuclear explosions on the Semipalatinsk test site. *Atomnaya Ehnergiya*, 67 (3):210–214, 1989. ISSN 0004-7163.

[7] G. Böttger, C. Denecke, R. Görner, M. Viehweg, H. Krause, and L. Schneider. Evaluation of the suitability of the sites and facilities at Degelen and Azgir in the Republic of Kazakhstan as a final repository for radioactive

waste. Technical Report EUR 17633, Office for Official Publications of the European Communities, Luxembourg, 1998.

[8] T. Caliński and J. Harabasz. A dendrite method for cluster analysis. *Commun. Stat.*, 3(1):1–27, 1974. ISSN 0090-3272. doi: 10.1080/03610927408827101.

[9] Y. Capdeville, P. Cupillard, and S. Singh. Chapter Six - An introduction to the two-scale homogenization method for seismology. In B. Moseley and L. Krischer, editors, *Advances in Geophysics*, volume 61 of *Machine Learning in Geosciences*, pages 217–306. Elsevier, 2020. doi: 10.1016/bs.agph.2020.07.001.

[10] E. Chaljub, P. Moczo, S. Tsuno, P.-Y. Bard, J. Kristek, M. Kaser, M. Stupazzini, and M. Kristekova. Quantitative Comparison of Four Numerical Predictions of 3D Ground Motion in the Grenoble Valley, France. *Bull. Seismol. Soc. Am.*, 100(4):1427–1455, 2010. ISSN 0037-1106. doi: 10.1785/0120090052.

[11] M. Cuturi. Fast Global Alignment Kernels. In *Proceedings of the 28th International Conference on Machine Learning*, Bellevue, WA, USA, 2011. Omnipress.

[12] D. L. Davies and D. W. Bouldin. A Cluster Separation Measure. *IEEE Trans. Pattern Anal. Mach. Intell.*, PAMI-1(2):224–227, 1979. ISSN 1939-3539. doi: 10.1109/TPAMI.1979.4766909.

[13] I. S. Dhillon, Y. Guan, and B. Kulis. Kernel k-means: Spectral clustering and normalized cuts. In *Proceedings of the Tenth ACM SIGKDD International Conference on Knowledge Discovery and Data Mining*, KDD '04, pages 551–556, New York, NY, USA, 2004. Association for Computing Machinery. ISBN 978-1-58113-888-7. doi: 10.1145/1014052.1014118.

[14] A. Douglas. P-signal complexity and source radiation patterns. VESIAC Report 7885-1-x, University of Michigan, 1967.

[15] W. Eaton, C. Haindl, and T. Nissen-Meyer. Seismic scattering regimes from multiscale entropy and frequency correlations. *Geophys. J. Int.*, 237(2):1109–1128, 2024. ISSN 0956-540X, 1365-246X. doi: 10.1093/gji/ggae098.

[16] T. G. Farr, P. A. Rosen, E. Caro, R. Crippen, R. Duren, S. Hensley, M. Kobrick, M. Paller, E. Rodriguez, L. Roth, D. Seal, S. Shaffer, J. Shimada, J. Umland, M. Werner, M. Oskin, D. Burbank, and D. Alsdorf. The Shuttle Radar Topography Mission. *Rev. Geophys.*, 45(2), 2007. ISSN 1944-9208. doi: 10.1029/2005RG000183.

[17] A. Frankel and W. Leith. Evaluation of topographic effects on P and S-waves of explosions at the northern Novaya Zemlya Test Site using 3-D numerical simulations. *Geophys. Res. Lett.*, 19(18):1887–1890, 1992. ISSN 00948276. doi: 10.1029/92GL02147.

[18] P. Gaebler, L. Ceranna, N. Nooshiri, A. Barth, S. Cesca, M. Frei, I. Grünberg, G. Hartmann, K. Koch, C. Pilger, J. O. Ross, and T. Dahm. A multi-technology analysis of the 2017 North Korean nuclear test. *Solid Earth*, 10(1):59–78, 2019. ISSN 1869-9529. doi: 10.5194/se-10-59-2019.

[19] S. Gaffet and B. Massinon. Far-field seismogram perturbations induced by topographic heterogeneity. *Geophys. Res. Lett.*, 24(24):3313–3316, 1997.

[20] E. Harrell and D. Hoffman. Plutonium Mountain. Inside the 17-year mission to secure a dangerous legacy of Soviet nuclear testing. Report by Project on Managing the Atom, Belfer Center for Science and International Affairs, John F. Kennedy School of Government, Harvard University, Cambridge, MA, 2013.

[21] W. Imperatori and P. Mai. The role of topography and lateral velocity heterogeneities on near-source scattering and ground-motion variability. *Geophys. J. Int.*, 202(3):2163–2181, 2015. ISSN 0956-540X, 1365-246X. doi: 10.1093/gji/ggv281.

[22] W. Imperatori and P. M. Mai. Broad-band near-field ground motion simulations in 3-dimensional scattering media. *Geophys. J. Int.*, 192(2):725–744, 2013. ISSN 0956-540X. doi: 10.1093/gji/ggs041.

[23] B. L. N. Kennett and E. R. Engdahl. Traveltimes for global earthquake location and phase identification. *Geophys. J. Int.*, 105(2):429–465, 1991. ISSN 1365-246X. doi: 10.1111/j.1365-246X.1991.tb06724.x.

[24] D. Komatitsch, Q. Liu, J. Tromp, P. Süss, C. Stidham, and J. H. Shaw. Simulations of Ground Motion in the Los Angeles Basin Based upon the Spectral-Element Method. *Bull. Seismol. Soc. Am.*, 94(1):187–206, 2004. ISSN 0037-1106. doi: 10.1785/0120030077.

[25] M. Kristeková, J. Kristek, and P. Moczo. Time-frequency misfit and goodness-of-fit criteria for quantitative comparison of time signals. *Geophys. J. Int.*, 178(2):813–825, 2009. ISSN 0956540X, 1365246X. doi: 10.1111/j.1365-246X.2009.04177.x.

[26] H. Kumagai, T. Saito, G. O'Brien, and T. Yamashina. Characterization of scattered seismic wavefields simulated in heterogeneous media with topography. *J. Geophys. Res. Solid Earth*, 116:B03308, 2011. ISSN 2156-2202. doi: 10.1029/2010JB007718.

[27] T. Lay. Analysis of near-source contributions to early P-wave coda for underground explosions. 3. Inversion for isotropic statterers. *Bull. Seismol. Soc. Am.*, 77(5):1767–1783, 1987.

[28] T. Lay and T. Zhang. Near-source contributions to teleseismic P waves and P-wave coda for underground explosions. *Bull. Seismol. Soc. Am.*, 82(1):383–405, 1992. ISSN 0037-1106.

[29] S.-J. Lee, D. Komatitsch, B.-S. Huang, and J. Tromp. Effects of Topography on Seismic-Wave Propagation: An Example from Northern Taiwan. *Bull. Seismol. Soc. Am.*, 99(1):314–325, 2009. ISSN 0037-1106. doi: 10.1785/0120080020.

[30] W. Leith. Degelen Nuclear Test and Tunnel Data. Technical Memorandum DNA001-95-C-1079, Defense Threat Reduction Agency, US Geological Survey, 1998.

[31] K. Leng, J. Korenaga, and T. Nissen-Meyer. 3-D scattering of elastic waves by small-scale heterogeneities in the Earth's mantle. *Geophys. J. Int.*, 223(1):502–525, 2020. ISSN 0956-540X. doi: 10.1093/gji/ggaa331.

[32] C. S. Lynnes and T. Lay. Inversion of P coda for isotropic scatterers at the Yucca Flat test site. *Bull. Seismol. Soc. Am.*, 79(3):790–804, 1989. ISSN 0037-1106.

[33] S. Ma, R. J. Archuleta, and M. T. Page. Effects of Large-Scale Surface Topography on Ground Motions, as Demonstrated by a Study of the San Gabriel Mountains, Los Angeles, California. *Bull. Seismol. Soc. Am.*, 97 (6):2066–2079, 2007. ISSN 0037-1106. doi: 10.1785/0120070040.

[34] F. Magnoni, E. Casarotti, A. Michelini, A. Piersanti, D. Komatitsch, D. Peter, and J. Tromp. Spectral-Element Simulations of Seismic Waves Generated by the 2009 L'Aquila Earthquake. *Bull. Seismol. Soc. Am.*, 104(1):73–94, 2014. ISSN 0037-1106. doi: 10.1785/0120130106.

[35] P. D. Marshall, D. Porter, and P. Peachell. Analysis of Seismograms from Nuclear Explosions of Known Yield at Degelen Mountain and Konystan in East Kazakhstan, USSR. Technical Report AWERE O 2/92, Atomic Weapons Research Establishment, Aldermaston, Berkshire, 1992.

[36] K. L. McLaughlin and R.-S. Jih. Scattering from near-source topography: Teleseismic observations and numerical simulations. *Bull. Seismol. Soc. Am.*, 78(4):1399–1414, 1988.

[37] R. A. Mueller and J. R. Murphy. Seismic characteristics of underground nuclear detonations, Part I: Seismic spectrum scaling. *Bull. Seismol. Soc. Am.*, 61(6):1675–1692, 1971.

[38] J. Paparrizos and L. Gravano. K-Shape: Efficient and Accurate Clustering of Time Series. *SIGMOD Rec.*, 45(1):69–76, 2016. ISSN 0163-5808. doi: 10.1145/2949741.2949758.

[39] S. Peacock, A. Douglas, and D. Bowers. Joint maximum-likelihood magnitudes of presumed underground nuclear test explosions. *Geophys. J. Int.*, 210(2):621–644, 2017. ISSN 0956-540X, 1365-246X. doi: 10.1093/gji/ggx130.

[40] N. A. Petersson and B. Sjogreen. *User's Guide to WPP Version 2.2*. Lawrence Livermore National Laboratory, Livermore, CA, 2013.

[41] M. Pienkowska. *Small-Scale Effects on Global Seismic Waves*. PhD thesis, University of Oxford / University of Oxford, 2019.

[42] M. Pienkowska, V. Monteiller, and T. Nissen-Meyer. High-frequency global wavefields for local 3-D structures by wavefield injection and extrapolation. *Geophys. J. Int.*, 225(3):1782–1798, 2021. ISSN 0956-540X, 1365-246X. doi: 10.1093/gji/ggaa563.

[43] B. Poursartip, A. Fathi, and L. F. Kallivokas. Seismic wave amplification by topographic features: A parametric study. *Soil Dyn. Earthq. Eng.*, 92:503–527, 2017. ISSN 0267-7261. doi: 10.1016/j.soildyn.2016.10.031.

[44] J. Ripperger, H. Igel, and J. Wasserman. Seismic wave simulation in the presence of real volcano topography. *Journal of Volcanology and Geothermal Research*, 128 (1-3):31–44, 2003. ISSN 03770273. doi: 10.1016/S0377-0273(03)00245-2.

[45] H. C. Rodean. Inelastic Processes in Seismic Wave Generation by Underground Explosions. In *Identification of Seismic Sources – Earthquake or Underground Explosions*, pages 97–189. D. Reidel Publishing Company, Dordrecht, Holland, 1981. ISBN 90-277-1320-0.

[46] A. J. Rodgers, N. A. Petersson, and B. Sjogreen. Simulation of topographic effects on seismic waves from shallow explosions near the North Korean nuclear test site with emphasis on shear wave generation. *J. Geophys. Res.*, 115:B11309, 2010. ISSN 0148-0227. doi: 10.1029/2010JB007707.

[47] P. J. Rousseeuw. Silhouettes: A graphical aid to the interpretation and validation of cluster analysis. *J. Comput. Appl. Math.*, 20:53–65, 1987. ISSN 0377-0427. doi: 10.1016/0377-0427(87)90125-7.

[48] E. Rygg. Anomalous Surface Waves from Underground Explosions. *Bull. Seismol. Soc. Am.*, 69(6):1995–2002, 1979.

[49] J. Schlittenhardt. The Effects of Spall on Teleseismic P-Waves: An Investigation With Theoretical Seismograms. In *Explosion Source Phenomenology*, pages 141–150. American Geophysical Union (AGU), 1991. ISBN 978-1-118-66382-0. doi: 10.1029/GM065p0141.

[50] R. Steinmann, L. Seydoux, É. Beaucé, and M. Campillo. Hierarchical Exploration of Continuous Seismograms With Unsupervised Learning. *J. Geophys. Res. Solid Earth*, 127(1):e2021JB022455, 2022. ISSN 2169-9356. doi: 10.1029/2021JB022455.

[51] J. L. Stevens and M. O'Brien. 3D Nonlinear Calculation of the 2017 North Korean Nuclear Test. *Seismol. Res. Lett.*, 89(6):2068–2077, 2018. ISSN 0895-0695. doi: 10.1785/0220180099.

[52] J. L. Stevens and T. W. Thompson. 3D Numerical Modeling of Tectonic Strain Release from Explosions. *Bull. Seismol. Soc. Am.*, 105(2A):612–621, 2015. ISSN 0037-1106, 1943-3573. doi: 10.1785/0120140125.

[53] S. Takemura, T. Furumura, and T. Maeda. Scattering of high-frequency seismic waves caused by irregular surface topography and small-scale velocity inhomogeneity. *Geophys. J. Int.*, 201(1):459–474, 2015. ISSN 1365-246X, 0956-540X. doi: 10.1093/gji/ggv038.

[54] H. Takenaka, B. L. N. Kennett, and H. Fujiwara. Effect of 2-D topography on the 3-D seismic wavefield using a 2.5-D discrete wavenumber-boundary integral equation method. *Geophys. J. Int.*, 124(3):741–755, 1996. ISSN 0956540X, 1365246X. doi: 10.1111/j.1365-246X.1996.tb05635.x.

[55] R. Tavenard, J. Faouzi, G. Vandewiele, F. Divo, G. Androz, C. Holtz, M. Payne, R. Yurchak, M. Rußwurm, K. Kolar, and E. Woods. Tslearn, A Machine Learning Toolkit for Time Series Data. *J. Mach. Learn. Res.*, 21 (118):1–6, 2020. ISSN 1533-7928.

[56] C. Trabant, C. Thurber, and W. Leith. Ground truth seismic events and location capability at Degelen mountain, Kazakhstan. *Phys. Earth Planet. Inter.*, 131:155–171, 2002.

[57] M. van Driel, L. Krischer, S. C. Stähler, K. Hosseini, and T. Nissen-Meyer. Instaseis: Instant global seismograms based on a broadband waveform database. *Solid Earth*, 6(2):701–717, 2015. ISSN 1869-9529. doi: 10.5194/se-6-701-2015.

[58] M. Weber, C. W. Wicks Jr., F. Krüger, G. Jahnke, and J. Schlittenhardt. Asymmetric radiation of seismic waves from an Atoll – Nuclear tests in French Polynesia. *Geophys. Res. Lett.*, 25(11):1967–1970, 1998. ISSN 1944-8007. doi: 10.1029/98GL51306.

[59] B. A. Young and R. E. Abbott. Recovery and Calibration of Legacy Underground Nuclear Test Seismic Data from the Leo Brady Seismic Network. *Seismol. Res. Lett.*, 91 (3):1488–1499, 2020. ISSN 0895-0695, 1938-2057. doi: 10.1785/0220190341.

[60] H. Zhou, J. Li, and X. Chen. Establishment of a seismic topographic effect prediction model in the Lushan Ms 7.0 earthquake area. *Geophys. J. Int.*, 221(1):273–288, 2020. ISSN 0956-540X. doi: 10.1093/gji/ggaa003.

# SUPPORTING INFORMATION FOR "RINGING MOUNTAIN RANGES: TELESEISMIC SIGNATURE OF THE INTERACTION OF HIGH-FREQUENCY WAVEFIELDS WITH NEAR-SOURCE TOPOGRAPHY AT THE DEGELEN NUCLEAR TEST SITE"

PREPRINT

**Marta Pienkowska**[1,2]**, Stuart E. J. Nippress**[3]**, David Bowers**[3]**, and Tarje Nissen-Meyer**[2,4]

[1]Department of Earth Sciences, ETH Zurich, Zurich, Switzerland.
[2]Department of Earth Sciences, University of Oxford, Oxford, UK.
[3]AWE Blacknest, Brimpton, Reading, UK.
[4]Department of Mathematics and Statistics and Joint Center of Excellence in Environmental Intelligence, University of Exeter, Exeter, UK

**Contents of this file**

1. Text S1 and S2
2. Figures S1 to S9
3. Tables S1 to S4
4. Caption for Dataset S1 (available for download)

***correspondence:** marta.pienkowska@erdw.ethz.ch

## Introduction

This document contains Supporting Information for the paper entitled "Ringing mountain ranges: Teleseismic signature of the interaction of high-frequency wavefields with near-source topography at the Degelen nuclear test site". For completeness, Text S1, along with a summary in Table 2, outlines the parametrisations of the tslearn [10] implementations of the time series clustering algorithms. Text S2 and Table 3 accompany the silhouette analysis in the main text and help evaluate the clustering results. Finally, Figures 1-4 complement Figure 3 in the main text; Figures 5-8 complement Figure 4 in the main text, while Figure 9 shows the modification of the topography for the purpose of the simulations in (a) and (b), as well as the setup of the coupled teleseismic simulations in (c).

### Text S1. Waveforms clustering with tslearn.

The following parameters need to be specified in tslearn [10] for both the kernel k-means with the Global Alignment Kernel [GAK, 3] and for the k-Shape [7] methods:

- The required number of clusters.
- The number of initialisations, that is, the number of times the k-means or the k-Shape algorithm is to be run with different centroid seeds. The final result is the best output of all consecutive runs in terms of inertia.
- The maximum number of iterations of the k-means or the k-Shape algorithm for a single run.
- The inertia variation threshold. If at some point inertia varies less than this threshold between two consecutive iterations, the model is considered to have converged and the algorithm stops.

We tested a range of convergence parameters (the number of initialisations and iterations, and the inertia threshold) for both methods to make sure that the results are stable. Table 2 summarises the convergence parameters used in the final clustering. Both algorithms were tested for 2 - 6 clusters for all stations to explore the dataset. Different time windows in the 0-20 s range were considered in all tests, from testing only the first arrivals (0-3s, 0-4s, 0-5s), through testing the first arrivals and the coda (0-10s, 0-15s, 0-20s), all the way to testing just the later arriving coda (3-20s, 4-20s, 5-20s).

In addition, the kernel k-means with the GA kernel requires the specification of the sigma, i.e. the bandwidth of the internal Gaussian kernel used for the GA kernel. The sigma scales the kernel (controls its width) to fit the data: if the bandwidth is too small, kernel densities overfit the data, while if it is too large, they underfit. The sigma values have been tested via trial-and-error, both manually for the 0.5-5 value range, as well as via the dedicated *sigma_gak* method provided in the tslearn package. Optimal sigma varies for the stations, but is of a similar order: EKA - 1.0; GBA - 1.5; YKA - 1.5; WRA - 1.8.

### Text S2. Evaluation of clustering results.

When the so-called ground truth is not known, evaluation of the results must be done using the model itself. In Table 3 we present a summary of three relevant scores that can be performed in that case: the Silhouette Coefficient [9], the Calinski-Harabasz Index [2] and the Davies-Bouldin Index [4]. The presented scores were calculated for the 20 second signals filtered at 2 Hz and 4 Hz. The indices show that GBA has the highest separation of the clusters, while EKA the lowest, which reflects the observed similarity of the waveforms in our visual analysis. Comparing the 2 Hz and 4 Hz coefficients for EKA is not meaningful, as the number of clusters changed, but all WRA indices show a better separation of clusters for the 4 Hz results. The GBA and YKA indices are relatively stable, although some improvement for the 4 Hz results is visible. That improvement did not impact the spatial delineation of the clusters. A detailed silhouette analysis is presented in the main text.

**Data Set S1.**

The data used in this study comprises waveforms recorded by four UK-design arrays – Gauribidanur (GBA), Eskdalemuir (EKA), Yellowknife (YKA) and Warramunga (WRA) – during the years 1964-1989. Tables 1 and 4 in this document summarise the dataset. The beamed waveform data are freely available for download from AWE Blacknest (`https://blacknest.gov.uk`).

Table 1: A summary of the data for the Degelen mountain events available at AWE Blacknest and used in this study. The table lists the total number of recorded events available per array, the number of events with end-of-adit locations available (published by Trabant et al. [11]), the number of events where only GPS locations are available (published by Leith [6], providing a less accurate location estimate than end-of-adit), as well as the number of events with depths and yields (published by Bocharov et al. [1]).

| Array | Total # of events | # of events with end-of-adit locations | # of events with GPS locations | # of events with known depths & yields |
|-------|---------|---------|---------|---------|
| GBA | 103 | 95 | 8 | 40 |
| EKA | 100 | 83 | 17 | 54 |
| YKA | 119 | 101 | 18 | 59 |
| WRA | 82 | 73 | 9 | 39 |

Table 2: A summary of the convergence parameters chosen for the tslearn [10] clustering algorithms: the kernel k-means with GAK [3] and the k-Shape [7].

| parameter | kernel k-means with GAK | k-Shape |
|-----------|---------|---------|
| # initialisations | 30 | 50 |
| max # iterations | 50 | 50 |
| inertia threshold | 1e-10 | 1e-7 |

Table 3: Summary of the Degelen clustering scores for three performance metrics: the Silhouette Coefficient score [9], the Calinski-Harabasz Index [2] and the Davies-Bouldin Index [4]. A higher Silhouette Coefficient score relates to a model with better defined clusters. Similarly, a higher Calinski-Harabasz score relates to a model with better defined clusters. For the Davies-Bouldin score, on the other hand, values closer to zero indicate a better partition (with zero being the lowest possible score). The scores listed in this table are for the k-Shape clustering of 20 second signals filtered up to 2 Hz and 4 Hz. A full Silhouette analysis (with coefficients for each sample) is shown in Figure 5 in the main text.

| Array | Silhouette Coefficient | | Calinski-Harabasz Index | | Davies-Bouldin Index | |
|-------|-------|-------|-------|-------|-------|-------|
| | 2 Hz | 4 Hz | 2 Hz | 4 Hz | 2 Hz | 4 Hz |
| GBA | 0.197 | 0.225 | 63.752 | 67.929 | 1.095 | 0.925 |
| EKA | 0.123 | 0.128 | 13.030 | 13.302 | 1.611 | 1.590 |
| YKA | 0.207 | 0.240 | 24.153 | 26.934 | 1.433 | 1.310 |
| WRA | 0.085 | 0.128 | 17.787 | 31.024 | 1.385 | 0.971 |

Table 4: A detailed summary of all data used for the analysis of source-side effects at the Degelen test site in Kazakhstan. End-of-adit latitudes and longitudes come from the study by Trabant et al. [11], whereas GPS locations are as reported by Leith [6]. Depths for pre-1972 events have been published by Bocharov et al. [1], and new body-wave magnitude ($m_b$) estimates have recently been published by Peacock et al. [8] (the $m_b$ values have been re-processed using the maximum-likelihood method which removes network bias). GBA, EKA, YKA and WRA stand for Gauribidanur, Eskdalemuir, Yellowknife and Warramunga, respectively, and the table indicates all recordings available for each array. The data from all four arrays span a total of a 137 events for years 1964-1989. For completeness and ease of cross-referencing, location IDs used in Trabant et al. [11] are included.

Due to its size, table 4 is included at the very bottom of this document.
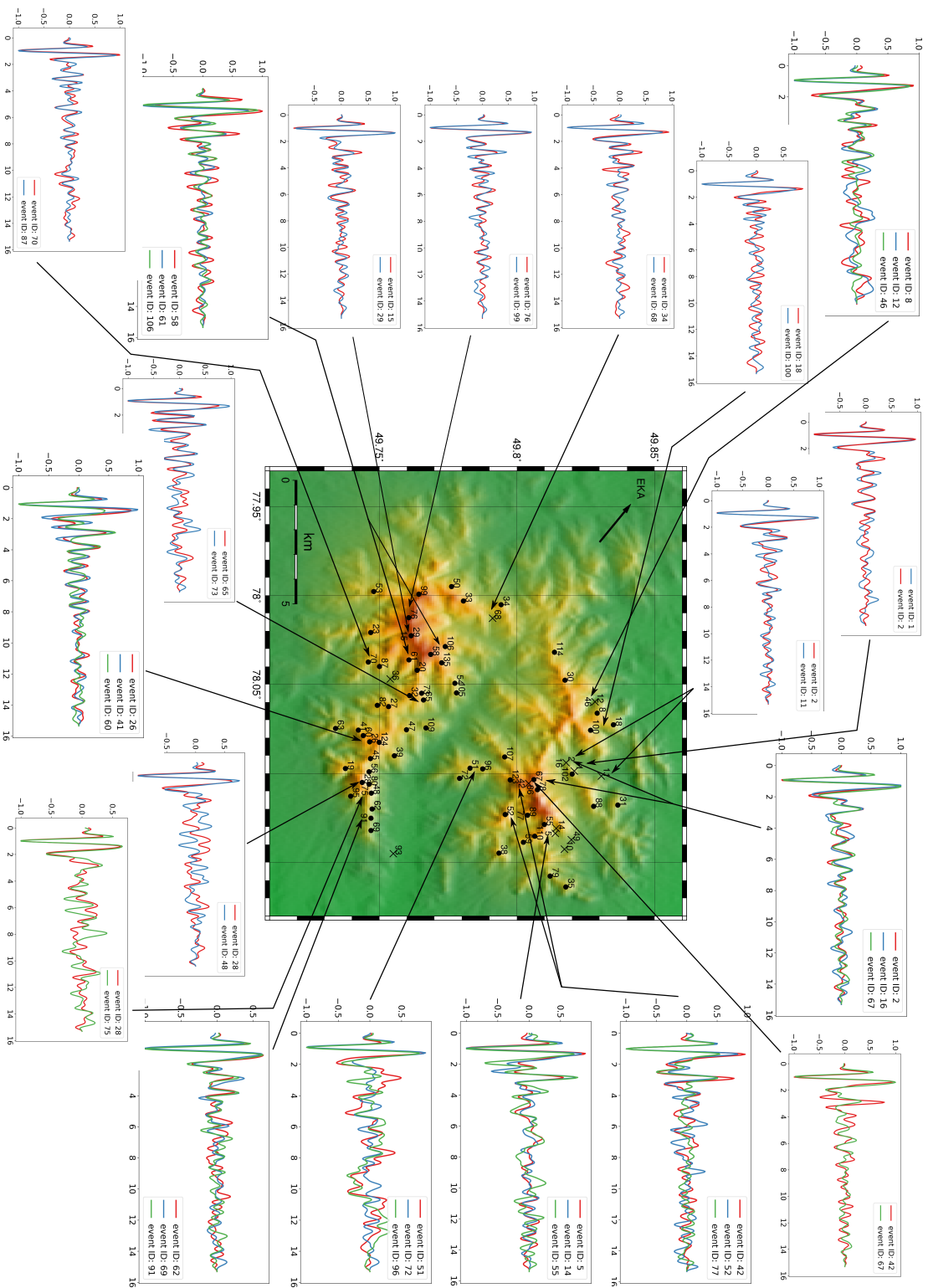
Figure 1: Location-dependent seismogram features at EKA low-pass filtered at 2 Hz. The direction from Degelen to EKA is indicated with an arrow. The adit ends corresponding to each event are plotted over the Degelen topography (circles). For events without adit-end locations, the GPS locations are shown (crosses). For better clarity the waveforms are cut at 15 s.
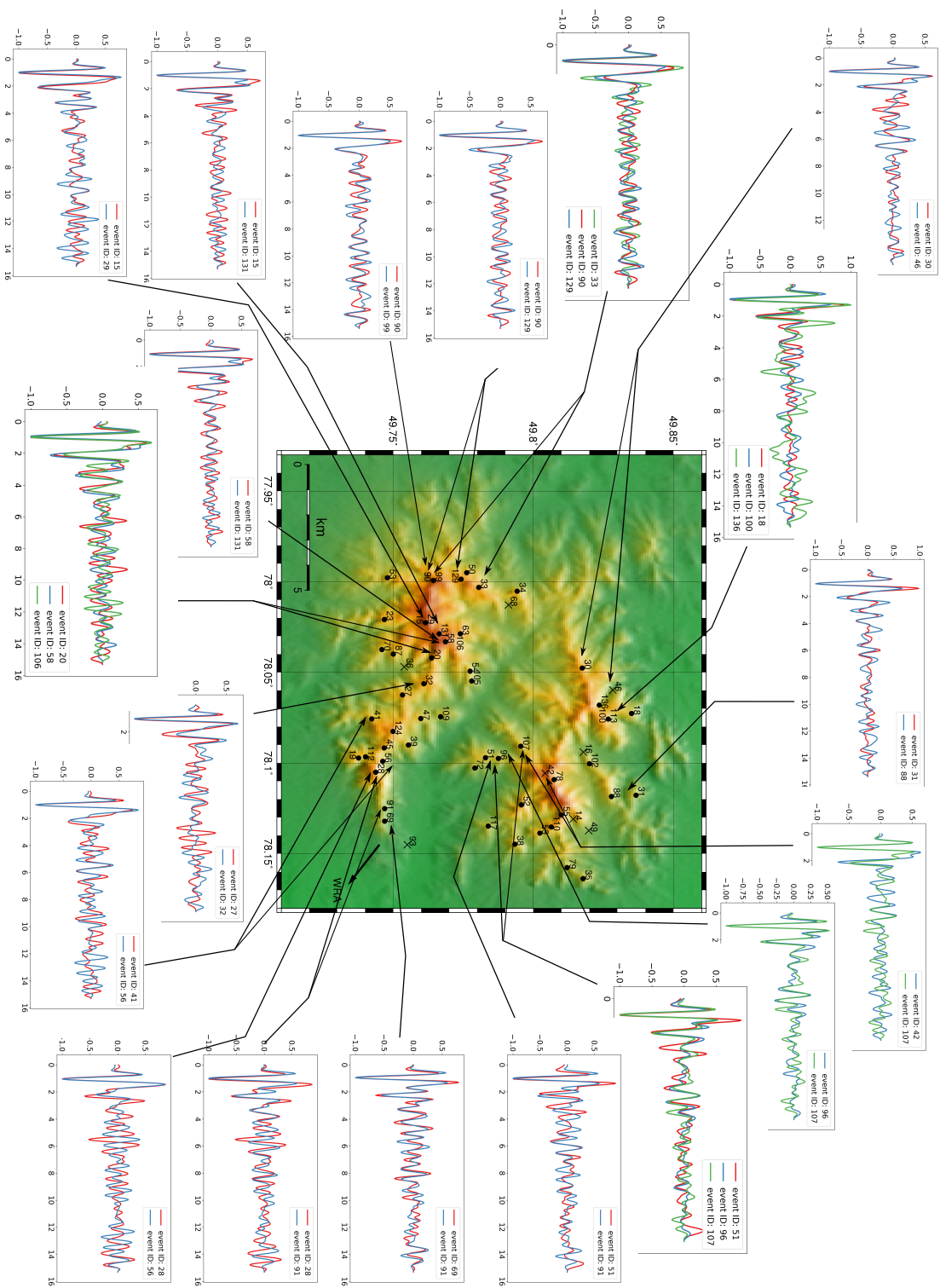
Figure 2: Location-dependent seismogram features at WRA low-pass filtered at 2 Hz. The direction from Degelen to WRA is indicated with an arrow. The adit ends corresponding to each event are plotted over the Degelen topography (circles). For events without adit-end locations, the GPS locations are shown (crosses). For better clarity the waveforms are cut at 15 s.

Figure 3: Location-dependent seismogram features at GBA low-pass filtered at 2 Hz. The direction from Degelen to GBA is indicated with an arrow. The adit ends corresponding to each event are plotted over the Degelen topography (circles). For events without adit-end locations, the GPS locations are shown (crosses). For better clarity the waveforms are cut at 15 s.
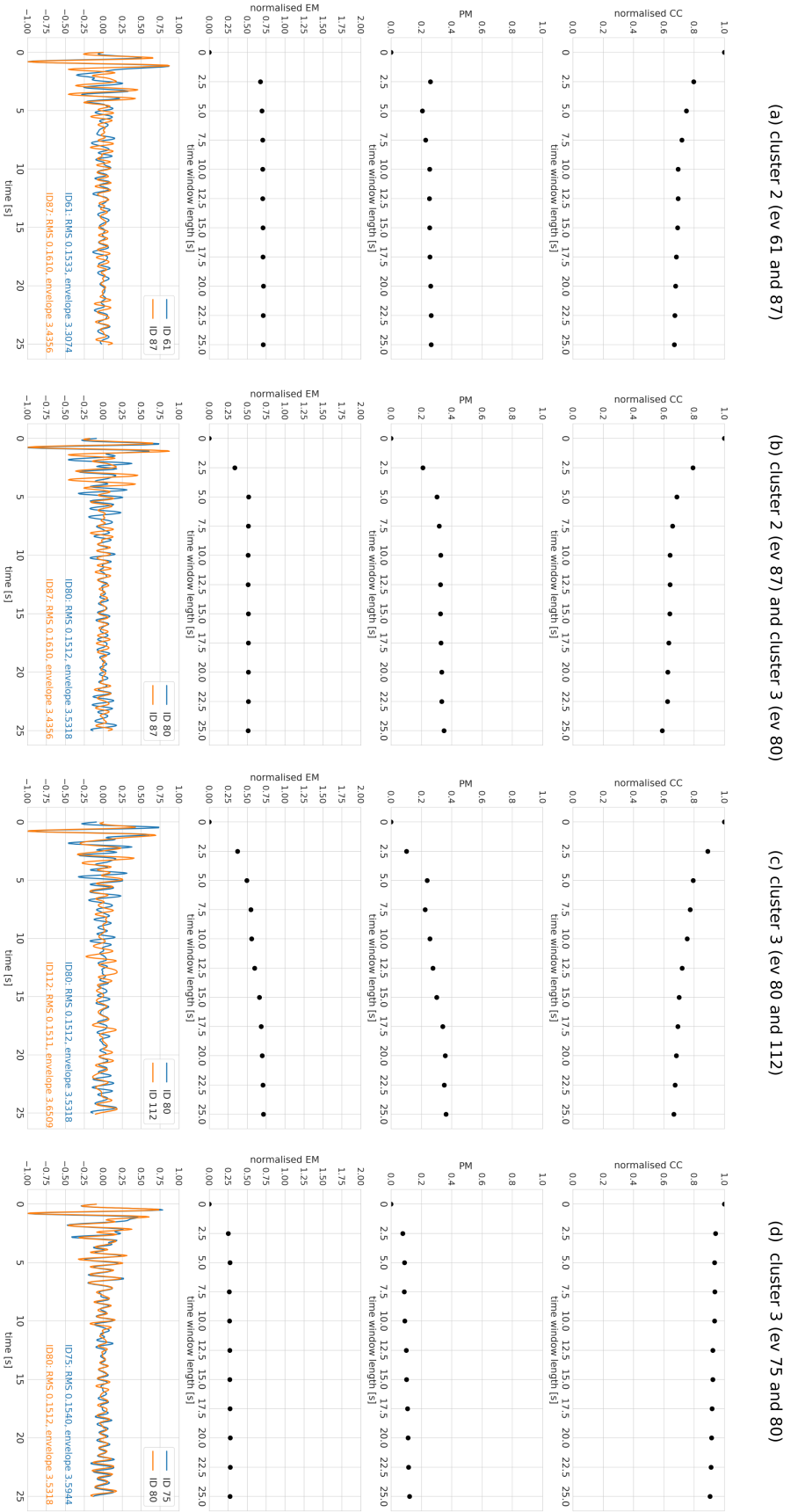
Figure 4: Examples of waveforms from cluster 2 and cluster 3 on the YKA array low-pass filtered at 2 Hz. In (a) two events from cluster 2 are compared: event 61 and event 87. In (b), event 87 from cluster 2 is compared to event 80 from cluster 3. In (c) and (d), event 80 from cluster 3 is compared with two other events from cluster 3, event 112 and event 75, respectively. All comparisons show the normalised cross-correlation (first row), the phase misfit (PM, second row), the normalised envelope misfit (EM, third row) for time-windows of increasing length, as well as a visual comparison between the waveforms along with the corresponding values for the RMS misfit (EM, third row) for time-windows of increasing length, as well as a visual comparison between the waveforms along with the corresponding values for the RMS and the area under the envelope (fourth row). The parameters average out the variations of the waveforms and mask the subtle differences.
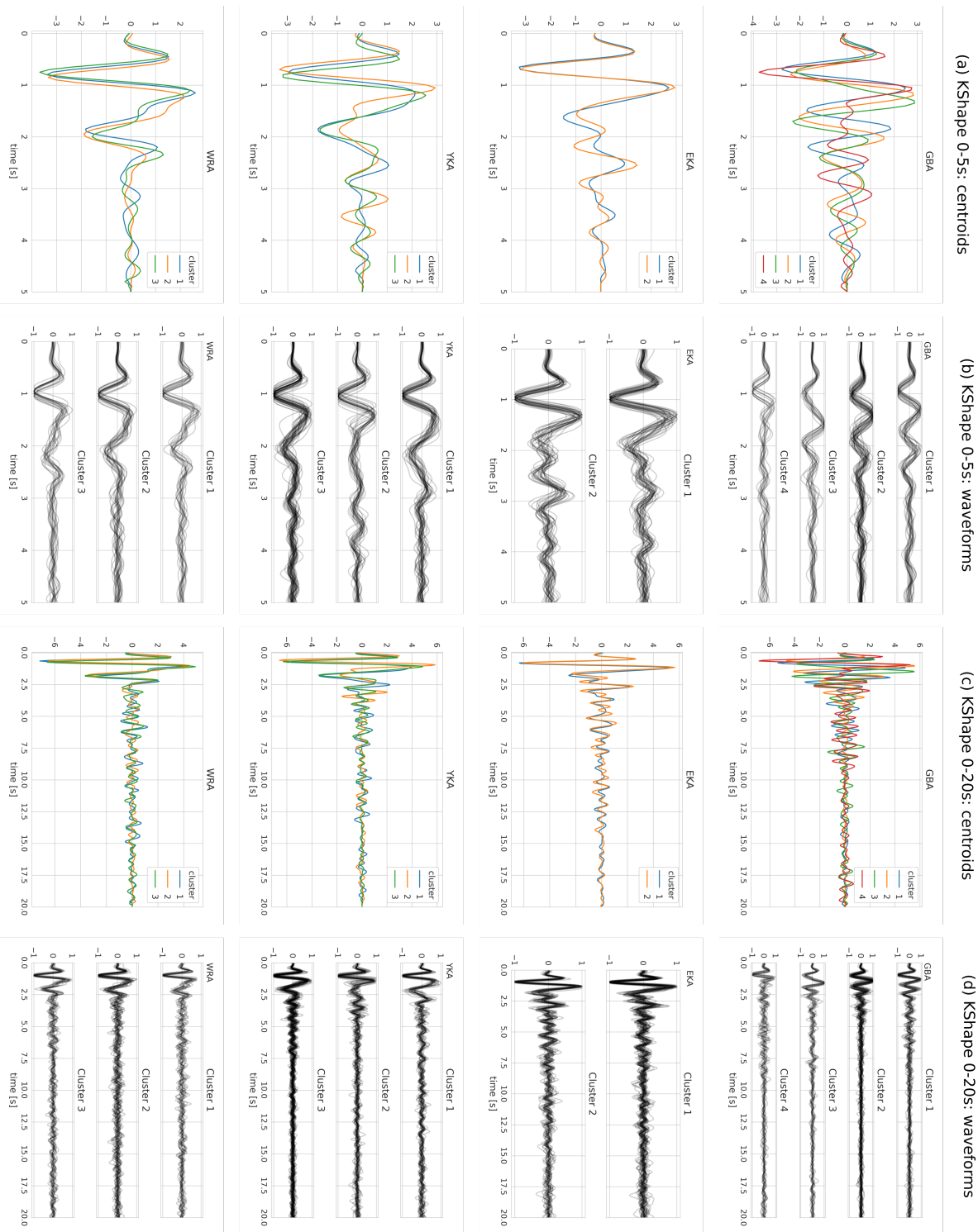
Figure 5: Waveforms and centroids for the clustering results for the k-Shape algorithm for waveforms low-pass filtered at 2 Hz. (a) The k-Shape centroids for each cluster for the 0-5 s time window. (b) The k-Shape waveforms assigned to each cluster for the 0-5 s time window. (c) The k-Shape centroids for each cluster for the 0-20 s time window. (d) The k-Shape waveforms assigned to each cluster for the 0-20 s time window.
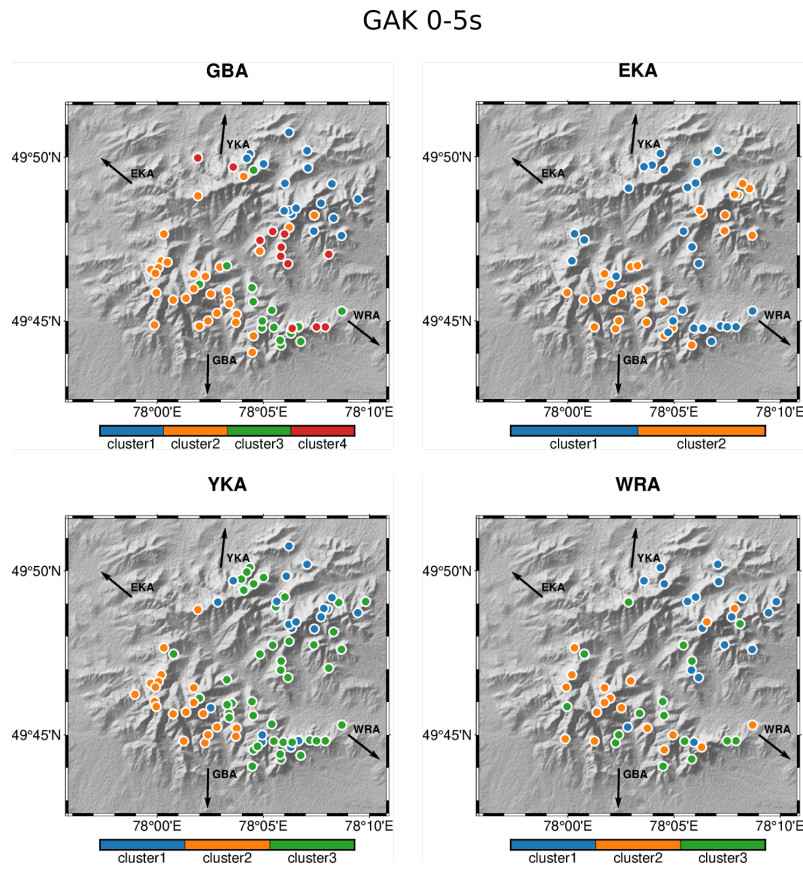
Figure 6: Clustering results for the Global Aligment Kernel (GAK) for the 0-5 s time window low-pass filtered at 2 Hz. The clusters correspond to the k-Shape results presented in Figure 4 in the main text. The GAK approach does not produce centroids and was unstable for time series beyond 100 samples (i.e. with cut-off longer than 5 s). Successfully employing GAK for the 0-5 s window, however, shows that the results indeed come from the data and are not biased by the algorithm.
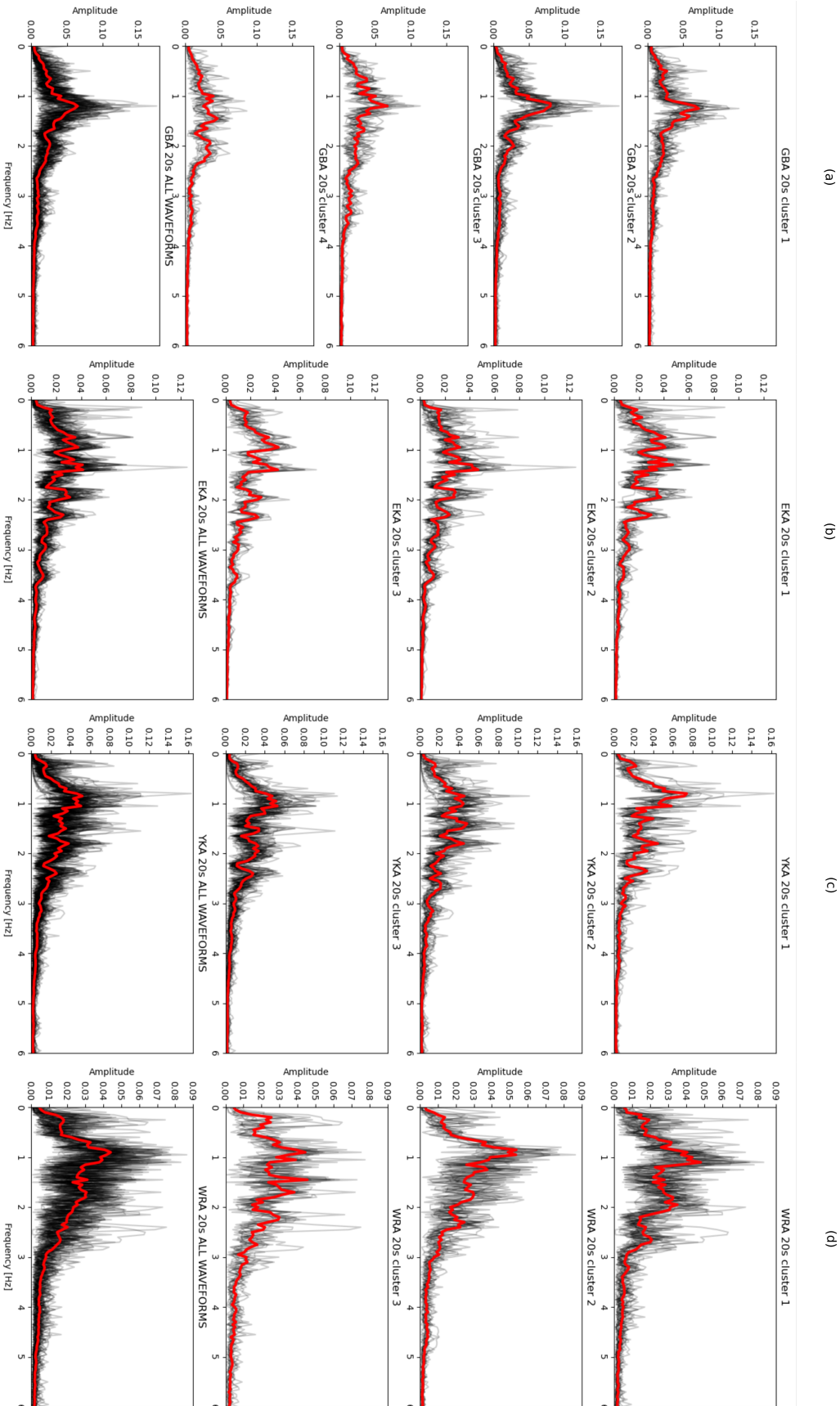
Figure 7: Spectra for the waveforms low-pass filtered at 4 Hz assigned to each cluster for (a) GBA, (b) EKA, (c) YKA, and (d) WRA. The plots in the last row include all waveforms for a given array. The red line shows the average for each plot.
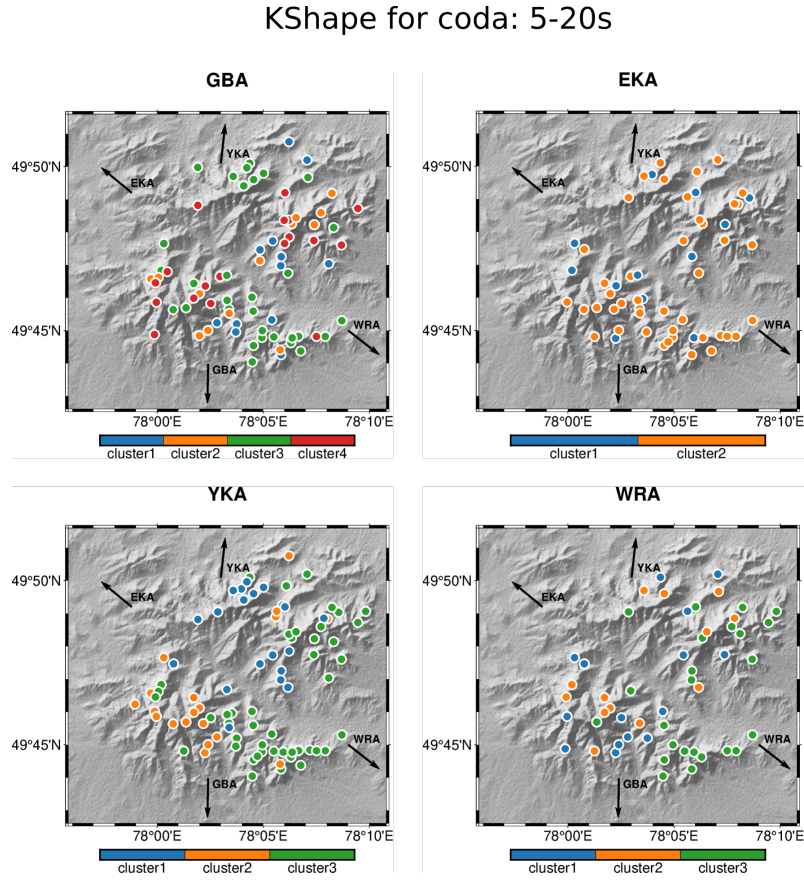
Figure 8: Clustering results for the coda waves in the 5-20 s time window low-pass filtered at 2 Hz. The spatial pattern for YKA corresponds to the 0-5 s and 0-20s time window clusters (see Figure 4 in the main text). No clear spatial patterns emerged for the 5-20 s coda waves recorded at GBA, EKA and WRA. With the location-based coherence of the later arrivals preserved only at YKA, it appears that the effect is direction- and/or take-off-angle-dependent. The same results were obtained for filtering up to 4 Hz.
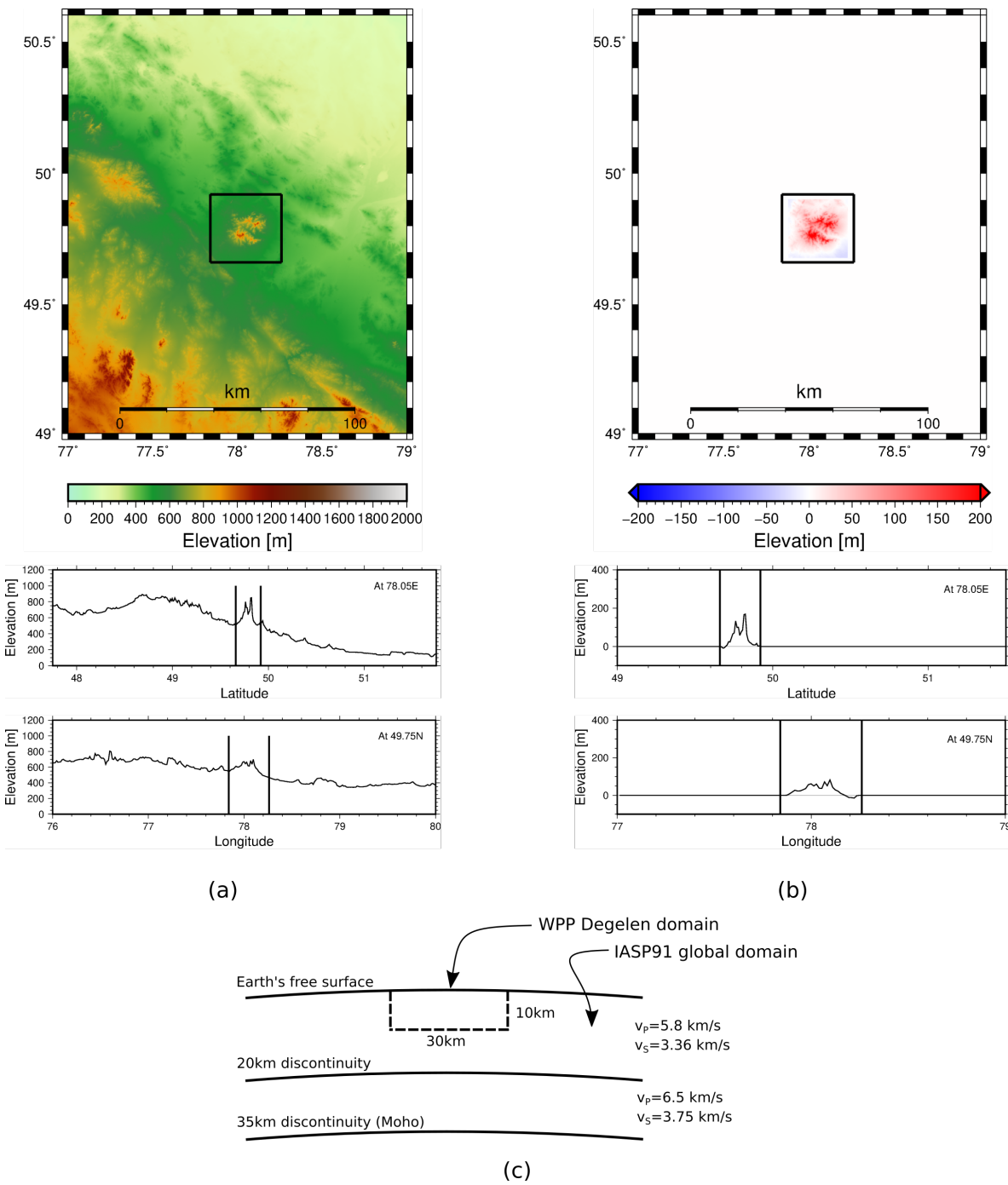
Figure 9: (a) The unmodified Degelen topography from the NASA's Shuttle Radar Topography Mission [SRTM, 5]. In the top panel the Degelen site is indicated by the black square of $30 \times 30$ km. The middle and bottom panels show cross sections at a longitude of 78.05 degrees East and at a latitude of 49.75 degrees North, respectively. (b) The modified Degelen topography with the top, middle and bottom panels corresponding to the panels in (a). The surrounding elevation and the underlying topographic trend are removed, so that the edges of the $30 \times 30$ km domain match the zero elevation of a spherical Earth. The modification is required for hybrid simulations at teleseismic distances. (c) A sketch of the proportions of the local Degelen domain with respect to global IASP91 discontinuities. The domain defined in WPP is $30 \times 30$ km wide and 10 km deep, and therefore remains in the homogeneous layer above the 20 km discontinuity of the IASP91 background model. The local domain dimensions and the discontinuity depths are shown to scale.

## REFERENCES

[1] V. S. Bocharov, S. A. Zelentsov, and V. N. Mikhajlov. Characteristics of the 96 underground nuclear explosions on the Semipalatinsk test site. *Atomnaya Ehnergiya*, 67(3):210–214, 1989. ISSN 0004-7163.

[2] T. Caliński and J. Harabasz. A dendrite method for cluster analysis. *Commun. Stat.*, 3(1):1–27, 1974. ISSN 0090-3272. doi: 10.1080/03610927408827101.

[3] M. Cuturi. Fast Global Alignment Kernels. In *Proceedings of the 28th International Conference on Machine Learning*, Bellevue, WA, USA, 2011. Omnipress.

[4] D. L. Davies and D. W. Bouldin. A Cluster Separation Measure. *IEEE Trans. Pattern Anal. Mach. Intell.*, PAMI-1(2): 224–227, 1979. ISSN 1939-3539. doi: 10.1109/TPAMI.1979.4766909.

[5] T. G. Farr, P. A. Rosen, E. Caro, R. Crippen, R. Duren, S. Hensley, M. Kobrick, M. Paller, E. Rodriguez, L. Roth, D. Seal, S. Shaffer, J. Shimada, J. Umland, M. Werner, M. Oskin, D. Burbank, and D. Alsdorf. The Shuttle Radar Topography Mission. *Rev. Geophys.*, 45(2), 2007. ISSN 1944-9208. doi: 10.1029/2005RG000183.

[6] W. Leith. Degelen Nuclear Test and Tunnel Data. Technical Memorandum DNA001-95-C-1079, Defense Threat Reduction Agency, US Geological Survey, 1998.

[7] J. Paparrizos and L. Gravano. K-Shape: Efficient and Accurate Clustering of Time Series. *SIGMOD Rec.*, 45(1):69–76, 2016. ISSN 0163-5808. doi: 10.1145/2949741.2949758.

[8] S. Peacock, A. Douglas, and D. Bowers. Joint maximum-likelihood magnitudes of presumed underground nuclear test explosions. *Geophys. J. Int.*, 210(2):621–644, 2017. ISSN 0956-540X, 1365-246X. doi: 10.1093/gji/ggx130.

[9] P. J. Rousseeuw. Silhouettes: A graphical aid to the interpretation and validation of cluster analysis. *J. Comput. Appl. Math.*, 20:53–65, 1987. ISSN 0377-0427. doi: 10.1016/0377-0427(87)90125-7.

[10] R. Tavenard, J. Faouzi, G. Vandewiele, F. Divo, G. Androz, C. Holtz, M. Payne, R. Yurchak, M. Rußwurm, K. Kolar, and E. Woods. Tslearn, A Machine Learning Toolkit for Time Series Data. *J. Mach. Learn. Res.*, 21(118):1–6, 2020. ISSN 1533-7928.

[11] C. Trabant, C. Thurber, and W. Leith. Ground truth seismic events and location capability at Degelen mountain, Kazakhstan. *Phys. Earth Planet. Inter.*, 131:155–171, 2002.

| event ID | Trabant et al location ID | GBA | EKA | YKA | WRA | date [yyyy:mm:dd] | time [hh:mm:ss] | mb | GPS latitude | GPS longitude | adit end latitude | adit end longitude | depth [km] |
|---|---|---|---|---|---|---|---|---|---|---|---|---|---|
| 1 | n/a | | x | x | | 1964-03-15 | 08:00:00 | 5.605 | 49.8208 | 78.0986 | n/a | n/a | 0.22 |
| 2 | n/a | | x | x | | 1964-05-16 | 06:01:00 | 5.594 | 49.8178 | 78.0939 | n/a | n/a | 0.253 |
| 3 | n/a | | x | x | | 1964-06-06 | 00:00:00 | 0 | 49.7747 | 77.9881 | n/a | n/a | n/a |
| 4 | n/a | | | x | | 1964-07-19 | 06:00:01 | 5.443 | 49.815 | 78.0931 | n/a | n/a | 1.68 |
| 5 | n/a | | x | x | | 1964-11-16 | 06:00:00 | 5.686 | 49.8139 | 78.1336 | n/a | n/a | 0.194 |
| 6 | 134 | | x | x | | 1965-02-04 | 06:00:00 | n/a | 49.7731 | 77.9914 | 49.7669 | 77.9979 | n/a |
| 7 | 134 | | x | x | | 1965-05-11 | 06:40:00 | 4.766 | 49.7731 | 77.9914 | 49.7669 | 77.9979 | 0.103 |
| 8 | 141 | | x | x | | 1965-06-17 | 03:45:00 | 5.257 | 49.8306 | 78.0578 | 49.8291 | 78.0661 | 0.152 |
| 9 | 135 | | | x | | 1965-07-29 | 03:05:00 | n/a | 49.785 | 77.9969 | 49.7784 | 78.0004 | 0.126 |
| 10 | n/a | | x | x | | 1965-09-17 | 04:00:00 | 5.223 | 49.8172 | 78.1425 | n/a | n/a | 0.156 |
| 11 | n/a | | x | x | | 1965-10-08 | 06:00:00 | 5.478 | 49.8306 | 78.1014 | n/a | n/a | 0.204 |
| 12 | n/a | | x | x | | 1965-11-21 | 04:58:00 | 5.656 | 49.8283 | 78.0597 | n/a | n/a | 0.278 |
| 13 | n/a | | | x | | 1965-12-24 | 05:00:00 | 4.97 | 49.8117 | 78.1075 | n/a | n/a | 0.213 |
| 14 | n/a | | x | x | x | 1966-02-13 | 04:58:00 | 6.276 | 49.8142 | 78.1308 | n/a | n/a | 0.297 |
| 15 | 3 | x | x | x | x | 1966-03-20 | 05:50:00 | 6.073 | 49.7517 | 78.0083 | 49.7615 | 78.0226 | 0.294 |
| 16 | n/a | | x | x | x | 1966-04-21 | 03:58:00 | 5.402 | 49.8178 | 78.0939 | n/a | n/a | 0.178 |
| 17 | 11 | x | x | x | x | 1966-05-07 | 03:58:00 | 4.748 | 49.7361 | 78.1072 | 49.7437 | 78.105 | 0.274 |
| 18 | 148 | x | x | | x | 1966-06-29 | 06:58:01 | 5.532 | 49.8392 | 78.0708 | 49.835 | 78.0726 | 0.187 |
| 19 | 10 | x | x | x | x | 1966-07-21 | 03:58:00 | 5.395 | 49.7356 | 78.1047 | 49.7376 | 78.0972 | 0.17 |
| 20 | 6 | x | x | x | x | 1966-08-05 | 03:58:00 | 5.425 | 49.7589 | 78.0486 | 49.7637 | 78.042 | 0.171 |
| 21 | n/a | x | x | x | | 1966-08-19 | 03:53:00 | 4.641 | 49.8306 | 78.1014 | n/a | n/a | 0.134 |
| 22 | 141 | | | x | x | 1966-09-07 | 03:52:00 | 4.627 | 49.8306 | 78.0578 | 49.8291 | 78.0661 | 0.117 |
| 23 | 4 | | x | x | x | 1966-10-19 | 03:58:00 | 5.712 | 49.7419 | 78.0256 | 49.7468 | 78.0208 | 0.185 |
| 24 | 5 | x | | x | | 1966-12-03 | 05:02:00 | 4.552 | 49.7403 | 78.0308 | 49.7473 | 78.0331 | 0.153 |
| 25 | 107 | x | | x | | 1967-01-30 | 04:02:00 | 4.666 | 49.7731 | 77.99 | 49.7705 | 77.9825 | 0.131 |
| 26 | 9 | x | x | x | | 1967-02-26 | 03:58:00 | 6.08 | 49.7394 | 78.0864 | 49.7464 | 78.0822 | 0.241 |
| 27 | 8 | x | x | x | x | 1967-03-25 | 05:58:01 | 5.354 | 49.7533 | 78.0536 | 49.7533 | 78.0624 | 0.152 |
| 28 | 11 | x | x | x | x | 1967-04-20 | 04:08:00 | 5.58 | 49.7361 | 78.1072 | 49.7437 | 78.105 | 0.225 |
| 29 | 3 | x | x | x | x | 1967-05-28 | 04:08:00 | 5.501 | 49.7517 | 78.0083 | 49.7615 | 78.0226 | 0.262 |
| 30 | 118 | x | x | x | x | 1967-06-29 | 02:57:00 | 5.339 | 49.8222 | 78.0433 | 49.8174 | 78.0476 | 0.195 |
| 31 | 101 | x | x | x | x | 1967-07-15 | 03:27:00 | 5.399 | 49.8442 | 78.1156 | 49.8366 | 78.1177 | 0.161 |
| 32 | 7 | x | x | x | x | 1967-08-04 | 06:58:00 | 5.337 | 49.7544 | 78.0503 | 49.7609 | 78.0562 | 0.16 |
| 33 | 137 | x | x | x | x | 1967-10-17 | 05:04:00 | 5.667 | 49.7844 | 77.9978 | 49.7805 | 78.0031 | 0.181 |
| 34 | 96 | x | x | x | x | 1967-10-30 | 06:04:00 | 5.444 | 49.7972 | 77.9994 | 49.7942 | 78.0052 | 0.173 |
| 35 | 102 | x | x | x | x | 1967-12-08 | 06:04:00 | 5.33 | 49.8183 | 78.1708 | 49.8177 | 78.1637 | 0.15 |
| 36 | n/a | x | x | x | x | 1968-01-07 | 03:47:00 | 5.005 | 49.7539 | 78.0469 | n/a | n/a | 0.237 |
| 37 | 100 | x | x | x | | 1968-04-24 | 10:36:00 | 4.91 | 49.8417 | 78.1072 | 49.8459 | 78.1035 | 0.127 |
| 38 | 110 | x | x | x | x | 1968-06-11 | 03:06:00 | 5.262 | 49.7986 | 78.15 | 49.7934 | 78.1447 | 0.148 |
| 39 | 113 | x | x | x | x | 1968-07-12 | 12:08:00 | 5.208 | 49.7556 | 78.0992 | 49.7554 | 78.09 | 0.172 |
| 40 | n/a | x | | | x | 1968-08-20 | 04:06:00 | 4.788 | 49.8206 | 78.0811 | n/a | n/a | 0.208 |
| 41 | 104 | x | x | x | x | 1968-09-01 | 04:06:00 | 5.472 | 49.7381 | 78.0808 | 49.7423 | 78.0756 | 0.162 |
| 42 | n/a | x | x | x | x | 1968-09-29 | 03:43:00 | 5.887 | 49.8042 | 78.1056 | n/a | n/a | 0.29 |
| 43 | 99 | x | | | x | 1968-10-29 | 03:54:00 | n/a | 49.8333 | 78.0928 | 49.831 | 78.0879 | n/a |
| 44 | 111 | x | | x | x | 1968-11-09 | 02:54:00 | 4.801 | 49.7997 | 78.1444 | 49.8007 | 78.1388 | 0.125 |
| 45 | 103 | x | x | x | x | 1968-12-18 | 05:02:00 | 5.066 | 49.7408 | 78.0878 | 49.7467 | 78.0916 | 0.194 |
| 46 | n/a | x | x | x | x | 1969-03-07 | 08:27:00 | 5.694 | 49.8283 | 78.0597 | n/a | n/a | 0.214 |
| 47 | 124 | x | x | x | x | 1969-05-16 | 04:03:00 | 5.279 | 49.7678 | 78.0817 | 49.7598 | 78.0754 | 0.184 |
| 48 | 125 | x | x | x | | 1969-07-04 | 02:47:00 | 5.268 | 49.7542 | 78.1092 | 49.747 | 78.111 | 0.219 |
| 49 | n/a | x | x | x | x | 1969-07-23 | 02:47:00 | 5.529 | 49.8197 | 78.1372 | n/a | n/a | 0.175 |
| 50 | 98 | x | x | x | x | 1969-09-11 | 04:02:00 | 4.951 | 49.7778 | 77.9864 | 49.7762 | 77.995 | 0.19 |
| 51 | 112 | x | x | x | x | 1969-10-01 | 04:03:00 | 5.275 | 49.7864 | 78.1081 | 49.7829 | 78.097 | 0.144 |
| 52 | 126 | x | x | x | x | 1970-01-29 | 07:03:00 | 5.624 | 49.7922 | 78.1131 | 49.7957 | 78.123 | 0.214 |
| 53 | 115 | x | x | | x | 1970-03-27 | 05:03:00 | 4.96 | 49.7444 | 78.0033 | 49.7479 | 77.9978 | 0.138 |
| 54 | 120 | x | x | | x | 1970-06-28 | 01:58:00 | 5.891 | 49.7822 | 78.0533 | 49.7774 | 78.0493 | 0.332 |
| 55 | 26 | x | x | x | x | 1970-07-24 | 03:57:00 | 5.353 | 49.8136 | 78.1322 | 49.8099 | 78.1286 | 0.154 |
| 56 | 78 | x | | x | x | 1970-12-17 | 07:01:00 | 5.447 | 49.7519 | 78.1017 | 49.7462 | 78.099 | 0.193 |
| 57 | 23 | x | | | | 1971-01-29 | 05:03:00 | n/a | 49.8053 | 78.1686 | 49.8039 | 78.1616 | n/a |
| 58 | 121 | x | x | x | x | 1971-04-25 | 03:33:00 | 6.084 | 49.7803 | 78.0367 | 49.7686 | 78.0331 | 0.296 |
| 59 | 25 | x | x | x | x | 1971-05-25 | 04:03:00 | 5.097 | 49.8042 | 78.145 | 49.8023 | 78.1386 | 0.132 |
| 60 | 16 | | x | x | | 1971-11-29 | 06:03:00 | 5.49 | 49.7378 | 78.0814 | 49.7441 | 78.0787 | 0.203 |
| 61 | 114 | | x | x | | 1971-12-30 | 06:21:00 | 5.868 | 49.755 | 78.0475 | 49.7607 | 78.0362 | 0.249 |
| 62 | 86 | | x | x | | 1972-03-10 | 04:57:00 | 5.487 | 49.7519 | 78.1181 | 49.7473 | 78.1199 | 0.171 |
| 63 | 76 | x | x | x | x | 1972-03-28 | 04:22:00 | 5.199 | 49.7342 | 78.0825 | 49.734 | 78.0747 | 0.124 |
| 64 | 145 | | x | x | | 1972-07-06 | 01:03:00 | 4.363 | 49.7361 | 78.1092 | 49.738 | 78.1097 | 0.081 |
| 65 | 123 | | x | x | | 1972-08-16 | 03:17:00 | 5.13 | 49.7706 | 78.0572 | 49.766 | 78.0587 | 0.139 |
| 66 | 11 | | x | x | | 1972-12-28 | 04:27:00 | n/a | 49.7361 | 78.1072 | 49.7437 | 78.105 | 0.132 |
| 67 | 22 | x | x | x | | 1973-02-16 | 05:03:00 | 5.509 | 49.8158 | 78.1067 | 49.8061 | 78.1034 | n/a |
| 68 | n/a | | x | x | x | 1973-07-10 | 01:27:00 | 5.353 | 49.7911 | 78.0128 | n/a | n/a | n/a |
| 69 | 89 | x | x | x | x | 1973-10-26 | 04:27:00 | 5.266 | 49.7522 | 78.1325 | 49.7469 | 78.132 | n/a |

| # | No. | A | B | C | D | Date | Time | Mag | Lat1 | Lon1 | Lat2 | Lon2 | |
|---|---|---|---|---|---|---|---|---|---|---|---|---|---|
| 70 | 65 | | x | x | x | 1974-05-16 | 03:03:00 | 5.276 | 49.7397 | 78.0358 | 49.7459 | 78.0374 | n/a |
| 71 | n/a | x | x | | | 1974-06-25 | 03:57:00 | 4.48 | 49.8306 | 78.1014 | n/a | n/a | n/a |
| 72 | 80 | x | x | x | x | 1974-07-10 | 02:57:00 | 5.201 | 49.7772 | 78.1125 | 49.7791 | 78.1027 | n/a |
| 73 | 68 | x | x | x | | 1974-09-13 | 03:03:00 | 5.176 | 49.7697 | 78.0553 | 49.7653 | 78.0549 | n/a |
| 74 | 45 | x | | | | 1974-12-16 | 06:41:00 | 4.969 | 49.8331 | 78.0267 | 49.8329 | 78.0318 | n/a |
| 75 | 13 | x | x | x | | 1975-03-11 | 05:43:00 | 5.454 | 49.7547 | 78.1075 | 49.7462 | 78.106 | n/a |
| 76 | 56 | x | x | x | | 1975-06-08 | 03:27:00 | 5.578 | 49.7517 | 78.0058 | 49.7606 | 78.0125 | n/a |
| 77 | 27 | x | x | x | | 1975-08-07 | 03:57:00 | 5.218 | 49.8019 | 78.1306 | 49.8038 | 78.1234 | n/a |
| 78 | 18 | x | x | x | x | 1975-12-13 | 04:57:00 | 5.026 | 49.8133 | 78.1086 | 49.8074 | 78.1091 | n/a |
| 79 | 24 | x | x | x | x | 1976-01-15 | 04:47:00 | 5.227 | 49.81 | 78.1714 | 49.812 | 78.1576 | n/a |
| 80 | 13 | x | x | x | | 1976-04-21 | 04:58:00 | 4.975 | 49.7547 | 78.1075 | 49.7462 | 78.106 | n/a |
| 81 | 54 | x | x | x | | 1976-05-19 | 02:57:00 | 4.761 | 49.7775 | 78.0156 | 49.777 | 78.0009 | n/a |
| 82 | 72 | x | x | x | | 1976-07-23 | 02:33:00 | 4.992 | 49.7433 | 78.0517 | 49.7492 | 78.0617 | n/a |
| 83 | 41 | x | | | | 1976-10-30 | 04:57:00 | 4.594 | 49.8314 | 78.0572 | 49.8285 | 78.0516 | n/a |
| 84 | 121 | x | | x | | 1976-12-30 | 03:57:00 | 5.113 | 49.7803 | 78.0367 | 49.7686 | 78.0331 | n/a |
| 85 | 122 | | x | | | 1977-03-29 | 03:57:00 | 0 | 49.7764 | 78.0175 | 49.7704 | 78.0136 | n/a |
| 86 | 18 | x | x | x | | 1977-04-25 | 04:07:00 | 5.108 | 49.8133 | 78.1086 | 49.8074 | 78.1091 | n/a |
| 87 | 64 | x | x | x | x | 1977-07-30 | 01:57:00 | 5.162 | 49.7506 | 78.0492 | 49.75 | 78.0399 | n/a |
| 88 | 21 | x | x | x | x | 1977-08-17 | 04:27:00 | 5.03 | 49.8308 | 78.1139 | 49.8278 | 78.1184 | n/a |
| 89 | 27 | x | x | x | | 1977-12-26 | 04:03:00 | 4.952 | 49.8019 | 78.1306 | 49.8038 | 78.1234 | n/a |
| 90 | 117 | x | | x | x | 1978-03-26 | 03:57:00 | 5.727 | 49.7619 | 77.9825 | 49.7643 | 77.9993 | n/a |
| 91 | 88 | x | x | x | x | 1978-04-22 | 03:07:00 | 5.369 | 49.7517 | 78.1317 | 49.7469 | 78.1251 | n/a |
| 92 | 34 | x | x | x | x | 1978-05-29 | 04:57:00 | 4.717 | 49.7914 | 78.0944 | 49.7986 | 78.1022 | n/a |
| 93 | n/a | x | x | x | x | 1978-07-28 | 02:47:00 | 5.766 | 49.755 | 78.145 | n/a | n/a | n/a |
| 94 | 110 | | | x | | 1978-09-20 | 05:03:00 | 4.287 | 49.7986 | 78.15 | 49.7934 | 78.1447 | n/a |
| 95 | 83 | x | x | x | | 1978-10-15 | 05:37:00 | 5.183 | 49.7367 | 78.1111 | 49.7395 | 78.1127 | n/a |
| 96 | 79 | x | x | x | x | 1978-10-31 | 04:17:00 | 5.281 | 49.7886 | 78.1075 | 49.7875 | 78.0974 | n/a |
| 97 | 22 | x | | x | x | 1978-12-14 | 04:43:00 | 4.76 | 49.8158 | 78.1067 | 49.8061 | 78.1034 | n/a |
| 98 | 127 | x | | | x | 1978-12-20 | 04:33:00 | 4.748 | 49.8108 | 78.0542 | 49.8169 | 78.0542 | n/a |
| 99 | 117 | x | x | x | x | 1979-05-06 | 03:17:00 | 5.255 | 49.7619 | 77.9825 | 49.7643 | 77.9993 | n/a |
| 100 | 35 | x | x | x | x | 1979-05-31 | 05:55:00 | 5.297 | 49.8342 | 78.0803 | 49.8267 | 78.0757 | n/a |
| 101 | 64 | x | | x | | 1979-09-27 | 04:13:00 | 4.459 | 49.7506 | 78.0492 | 49.75 | 78.0399 | n/a |
| 102 | 30 | x | x | x | x | 1979-10-18 | 04:17:00 | 5.268 | 49.8242 | 78.0975 | 49.82 | 78.1003 | n/a |
| 103 | 77 | x | | | x | 1979-11-30 | 04:53:01 | 4.462 | 49.7831 | 78.0867 | 49.7794 | 78.0953 | n/a |
| 104 | 126 | | x | x | x | 1979-12-21 | 04:42:00 | 4.762 | 49.7922 | 78.1131 | 49.7957 | 78.123 | n/a |
| 105 | 70 | x | x | x | x | 1980-04-10 | 04:07:00 | 5.023 | 49.7825 | 78.0572 | 49.778 | 78.0547 | n/a |
| 106 | 63 | x | x | x | x | 1980-05-22 | 03:57:00 | 5.567 | 49.7797 | 78.0364 | 49.7739 | 78.0287 | n/a |
| 107 | 133 | x | x | x | x | 1980-07-31 | 03:33:00 | 5.369 | 49.7906 | 78.0908 | 49.7955 | 78.0907 | n/a |
| 108 | 142 | x | x | | x | 1980-09-25 | 06:21:13 | 4.875 | 49.7833 | 78.0806 | 49.7855 | 78.0805 | n/a |
| 109 | 74 | x | x | x | x | 1981-06-30 | 01:57:15 | 5.202 | 49.7675 | 78.0808 | 49.7669 | 78.0744 | n/a |
| 110 | 17 | | x | | x | 1981-07-17 | 02:37:18 | 5.121 | 49.8014 | 78.1314 | 49.8064 | 78.1352 | n/a |
| 111 | 71 | x | x | x | x | 1981-08-14 | 02:27:15 | 4.925 | 49.7522 | 78.0531 | 49.7587 | 78.0565 | n/a |
| 112 | 14 | x | | x | x | 1981-11-20 | 04:57:05 | 5.059 | 49.7367 | 78.1042 | 49.7401 | 78.0965 | n/a |
| 113 | 35 | x | | x | x | 1981-12-22 | 04:31:05 | 5.001 | 49.8342 | 78.0803 | 49.8267 | 78.0757 | n/a |
| 114 | 46 | x | x | x | | 1982-02-19 | 03:56:13 | 5.435 | 49.8233 | 78.0333 | 49.8136 | 78.0319 | n/a |
| 115 | 81 | x | x | x | x | 1982-06-25 | 02:03:07 | 4.637 | 49.7714 | 78.1108 | 49.7749 | 78.0996 | n/a |
| 116 | 5 | x | x | x | | 1982-08-23 | 02:43:08 | 4.531 | 49.7403 | 78.0308 | 49.7473 | 78.0331 | n/a |
| 117 | 87 | x | | x | x | 1982-09-21 | 02:57:03 | 5.201 | 49.7792 | 78.1247 | 49.7839 | 78.1347 | n/a |
| 118 | 62 | | | x | | 1982-12-25 | 04:23:08 | 4.544 | 49.7811 | 78.035 | 49.7763 | 78.028 | n/a |
| 119 | 66 | | | x | x | 1983-03-30 | 04:17:10 | 4.692 | 49.785 | 78.0406 | 49.781 | 78.0413 | n/a |
| 120 | 73 | x | | x | x | 1983-04-12 | 03:41:08 | 4.719 | 49.7856 | 78.0847 | 49.791 | 78.0807 | n/a |
| 121 | 65 | | x | | | 1983-06-24 | 02:56:14 | 4.544 | 49.7397 | 78.0358 | 49.7459 | 78.0374 | n/a |
| 122 | 143 | x | | x | x | 1983-09-11 | 06:33:13 | 4.559 | 49.7847 | 78.0842 | 49.7854 | 78.0806 | n/a |
| 123 | 31 | x | x | x | | 1983-12-26 | 04:29:09 | 5.527 | 49.79 | 78.1092 | 49.7975 | 78.1036 | n/a |
| 124 | 75 | x | x | x | x | 1984-04-15 | 03:17:11 | 5.732 | 49.7606 | 78.0892 | 49.7499 | 78.0825 | n/a |
| 125 | 33 | x | | | x | 1984-09-09 | 02:59:09 | 4.949 | 49.8044 | 78.0875 | 49.806 | 78.0997 | n/a |
| 126 | 128 | x | | | | 1984-11-23 | 03:55:08 | 4.41 | 49.8125 | 78.0594 | 49.8176 | 78.0551 | n/a |
| 127 | n/a | x | | | | 1985-07-25 | 03:11:09 | 4.873 | 49.8192 | 78.1494 | n/a | 0 | n/a |
| 128 | 32 | x | | x | | 1987-02-26 | 04:58:24 | 5.327 | 49.8342 | 78.0811 | 49.8299 | 78.0835 | n/a |
| 129 | 55 | x | | x | x | 1987-05-06 | 04:02:08 | 5.602 | 49.7758 | 78.0122 | 49.7742 | 77.9986 | n/a |
| 130 | 37 | x | | x | | 1987-06-06 | 02:37:09 | 5.38 | 49.8367 | 78.0617 | 49.8327 | 78.0704 | n/a |
| 131 | 57 | x | | x | x | 1987-07-17 | 01:17:09 | 5.945 | 49.7758 | 78.0197 | 49.7664 | 78.0287 | n/a |
| 132 | 55 | | | x | x | 1987-12-20 | 02:55:09 | 4.514 | 49.7758 | 78.0122 | 49.7742 | 77.9986 | n/a |
| 133 | 119 | x | | x | x | 1988-04-22 | 09:30:09 | 4.724 | 49.7903 | 78.1069 | 49.7942 | 78.1 | n/a |
| 134 | 12 | x | x | x | x | 1988-10-18 | 03:40:09 | 4.728 | 49.78 | 78.0172 | 49.7799 | 78.0079 | n/a |
| 135 | 58 | x | x | x | | 1988-11-23 | 03:57:09 | 5.277 | 49.7794 | 78.0372 | 49.7726 | 78.0378 | n/a |
| 136 | 38 | x | | x | x | 1989-02-17 | 04:01:09 | 4.973 | 49.8278 | 78.0597 | 49.8235 | 78.068 | n/a |
| 137 | 60 | x | | | | 1989-10-04 | 11:30:00 | 4.475 | 49.7483 | 78.0094 | 49.7498 | 78.0117 | n/a |